UNIVERSITY OF CALIFORNIA, MERCED

MICROSTRUCTURE OPTICAL FIBER BASED PARAMETRIC DEVICES AND APPLICATIONS TO COHERENT RAMAN SCATTERING MICROSCOPY AND ENTANGLED PHOTON PAIR GENERATION

A DISSERTATION
SUBMITTED TO THE SCHOOL OF NATURAL SCIENCES
AND THE DIVISION OF GRADUATE STUDIES
OF UNIVERSITY OF CALIFORNIA, MERCED
IN PARTIAL FULFILLMENT OF THE REQUIREMENTS
FOR THE DEGREE OF
DOCTOR OF PHILOSOPHY

by

Leily S. Kiani
December 2015

I certify that I have read this dissertation and that, in my opinion, it is fully adequate in scope and quality as a dissertation for the degree of Doctor of Philosophy.

(Professor Jay E. Sharping) Principal Advisor

I certify that I have read this dissertation and that, in my opinion, it is fully adequate in scope and quality as a dissertation for the degree of Doctor of Philosophy.

(Professor Michael Scheibner) Committee Chair

I certify that I have read this dissertation and that, in my opinion, it is fully adequate in scope and quality as a dissertation for the degree of Doctor of Philosophy.

(Professor Jennifer Lu)

I certify that I have read this dissertation and that, in my opinion, it is fully adequate in scope and quality as a dissertation for the degree of Doctor of Philosophy.

(Professor Jing Xu)

Approved for the University of California, Merced Graduate Studies

_____

Preface

It is truly a remarkable time to be a member of the global photonics community. 2015 is deemed the International Year of Light and Light-based Technologies by the United Nations to recognize and raise awareness of how optical technologies promote sustainable development and provide solutions to worldwide challenges in energy, education, agriculture, communications and health. [1] The most brilliant light on Earth is laser light [2]. With the unique properties of high coherence and monochromaticity, lasers have enabled a wide variety of impactful scientific and industrial technologies. The list of laser applications is expansive, but some notable applications include spectroscopy and microscopy, communications, data storage and retrieval, welding and ablation, photochemistry, ultra-cold physics, quantum physics, nuclear fusion, LIDAR, optical tweezers and photolithography. This dissertation aims to summarize five years of work on fiber-based parametric light sources. The inclusion of work regarding classical and quantum applications highlights the broad applicability of these devices.

To my grandmothers, two inspiring thinkers.

If a tree could fly off, it would not suffer the saw.
The sun hurries all night to be back for morning.
Salty water rises in the air,
so the garden will be drenched with fresh rain.

A drop leaves home,
enters a certain shell, and becomes a pearl.
Joseph turns from his weeping father, toward Egypt.
Remember how that turned out.

Journeys bring power and love back into you.
If you cannot go somewhere,
move in the passageways of the self.

They are like shafts of light, always changing,
and you change when you explore them.

-Rumi

Acknowledgments

This dissertation is the result of countless hours of mentorship, discussions with colleagues, collaborations and backing from my family and friends. I would like to extend deep gratitude to my mentor and advisor Prof. Jay Sharping for his wisdom, endless support and unshakable patience. He has done so much more than allow me to pursue my research interests. His efforts in teaching me how to be a scientist have brought me eons ahead of where I started.

The members of my dissertation committee, Prof. Michael Scheibner, Prof. Jing Xu and Prof. Jennifer Lu, have kept me on track to complete this dissertation and offered their invaluable guidance in my research and beyond. I thank them for having an open-door policy with me. I would also like to thank the collaborators and colleagues that have contributed to the success of this dissertation, Prof. Sharaam Afshar, Tilanka Munasinghe, Prof. Kristan Corwin and Prof. Brian Washburn. I would like to give special thanks to Thompson Lu who I had the great pleasure of working with on our most fruitful projects. I am so grateful that I had the opportunity to collaborate with and befriend Thompson. For their moral support, cooperative nature, helpful feedback and occasional proofreading of emails I thank the past and present lab members in our research group, Tessa Pinon, Chenji Gu, Alessandro Castelli, Alison Huff, Jacob Pate and Rodolfo Lopez. I also acknowledge the helpful undergraduates that I have worked with, Michael Lum, Michael Lee and Elizabeth Mercado.

There are of course people who influenced this dissertation that did were not directly involved in the research. I would like to mention the mentorship and support

I received from Dr. Carrie Menke. I am immensely grateful to Patrick Barnes for his support throughout the entirety of my graduate studies, especially through the most stressful times. For their understanding, kindness and encouragement I thank Cyprian Czarnocki, Dana Burow, Makiko Tsukamoto Quint and David Quint. I especially thank Jessica Romo for being an integral part of my pursuit of graduate studies.

Finally I would like to express my deepest appreciation toward my parents Mehrdad and Mitra and my sister Naria for their inspiration, sacrifice, patience and love.

Contents

List of Figures

Chapter 1

Introduction

1.1 Tunable light sources

Laser light sources often derive their utility from the ability to probe the narrow linewidth resonances in the material of the natural world. The matching of the light frequency to these resonances allows for the fine measurement of composition and transitions in materials. Laser light sources that are broad and/or tunable in frequency can thus be useful in a wide variety of spectroscopic applications. Certainly the major effort in nonlinear optics since its beginnings in the 1960s has been to generate spectral broadening and new frequency components. Today there exists a wealth of nonlinear crystals, optical fibers, pump laser sources and nonlinear processes from which to develop spectrally agile light sources.

The applications of tunable light sources are vast and continuing to grow. Spectroscopy, microscopy and imaging applications include: spontaneous Raman scattering (SRS), coherent anti-Stokes Raman scattering (CARS), two-photon fluorescence (2PA), second harmonic generation (SHG), third harmonic generation (THG), fluorescence lifetime experiments, confocal implementations, optical coherence tomography (OCT), etc. Telecommunications applications include: multi-wavelength dense wavelength division multiplexers (DWDMs), ultrafast all-optical signal processing, etc. Quantum information applications include: high fidelity sources for heralded single photons, quantum frequency conversion, generation of narrow-band pure states, etc.

Metrology applications include: optical clocks, absolute frequency metrology, etc. Clinical applications include: flow cytometry, targeted drug delivery, light therapies, etc. Other applications or enabled projects include: pulse generation, pulse compression, optical fiber testing, fs laser pulse stabilization, high speed and long haul transmission systems and more.

Each application requires different source parameters. The wide array of available combinations of lasers and nonlinear optical gain media produces potential sources over a range of pulse durations, pulse energies, linewidths and tunability ranges. Narrow linewidth continuous wave lasers are in the kHz range [3]. Ultrafast laser pulses have been achieved into the attosecond range [4, 5]. Pulse energies as high as 8 millijoules have been generated [6]. Supercontinua in the range of 1μ m can routinely be generated over an octave in frequency [7]. Tunability of optical parametric oscillators is in the range of hundreds of GHz [8, 9]. It is however important to combine and balance these attributes for customized light sources in the wide range of applications explained above. Dexterity in the tunability of these attributes enables complex spectroscopic measurements.

The purpose of this dissertation work is to improve two applications of tunable light sources with fiber optical parametric oscillators based on microstructure optical fibers: CARS microscopy and single photon sources.

CARS Microscopy

Microscopy of live cells is a vigorous area of research and is mostly enabled by fluorescent labeling of molecules of interest. While fluorescence microscopy has facilitated a vast number of biological discoveries, there are drawbacks to adding labels to the live environment. Fluorescent labels likely interact with the local environment and especially disrupt the physiology of smaller molecules like cholesterols [10]. Label-free spectroscopy based on Raman scattering has been explored as a way to overcome this limitation. Raman scattering reveals the vibrational fingerprint of molecules and can thus be chemical-specific to any molecule while being label-free.

Coherent Raman scattering spectroscopy techniques make it possible to probe the low frequency nuclear vibrations of materials using high frequency fields. The energy

conservation relationship between these frequencies is given by

$$\Delta\omega = \omega_1 - \omega_2 = \Omega \tag{1.1}$$

where ω_1, ω_2 are the frequencies of two incident light fields and Ω is the materials vibrational response frequency. Chemical specificity in this scattering process is derived from tuning, the difference between ω_1 and ω_2, to a particular Raman vibrational mode of the material of interest. Let the frequency of that vibrational mode be represented as Ω, so the following energy level diagrams in figure 1.1 represent the spontaneous and coherent Raman interactions.

If another pump photon enters the process, the system can produce a higher energy photon. Taking ω_1, ω_2 to be a pump photon, ω_p and a red shifted Stokes photon, ω_s respectively the energy conservation relationship becomes

$$\omega_{as} = 2\omega_p - \omega_s \tag{1.2}$$

where ω_{as} is a higher energy, anti-Stokes photon. The Raman vibrational level $|v = 1\rangle$ mediates the level to which the second pump photon scatters which in turn determines the scattered anti-Stokes frequency ω_{as}. The spontaneously scattered anti-Stokes photon frequency ω_{as} is the detected field, it indicates the Raman vibrational frequency giving chemical specificity to the measurement.

CARS microscopy requires dexterous wavelength tuning in order to probe the wide variety of vibrational modes relevant to cell biology. The other specifications for an ideal CARS microscopy light source include relatively high power (1 kW peak power), narrow spectrum pulses (1 nm) which are thus limited in duration (1 ps) and sufficient spectral brightness (10 mW/nm) [10]. Due to the label-free chemical specificity of the technique, the development of a lightweight, easy-to-use source for coherent Raman scattering spectroscopy has a suite of implications for advancing biophotonics, clinical photonics, atmospherics and space exploration.

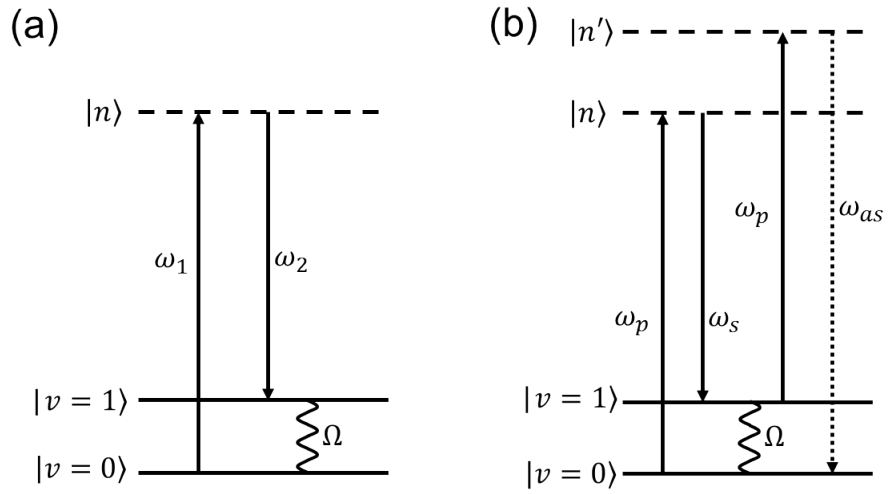

Figure 1.1: (a) The spontaneous Raman scattering process where two photons, ω_1 and ω_2, are coherently drive the Raman vibration Ω. (b) The coherent anti-Stokes Raman scattering process where two pump photons, $2\omega_p$, and a Stokes photon, ω_s, coherently drive the system to scatter an anti-Stokes photon ω_{as}.

Single photon sources

One giant leap in human understanding of light comes from the treatment of light as an ensemble of constituent fragments [11]. If light is considered to be made up of fragments then those fragments are readily describable in the language of quantum mechanics. These fragments are referred to as photons but the task of defining what exactly is a photon has been a tricky one [12, 13]. Nevertheless there is unequivocal evidence of quantum mechanical light particles [14, 15]. Producing, controlling and manipulating photons in a way that preserves their quantum mechanical nature is an active area of research [16].

The major application of single photon sources and detectors is to quantum information science. Photons are amenable to implementations as qubits, where information is encoded into the polarization, momentum, energy, spatial mode etc., because they travel at the speed of light and they interact weakly with their environment. Another possible vehicle for encoding information is in the photon number statistics of a stream of photons. An extreme notion of photon number statistics is the concept of a single photon.

The ideal source of single photons is one that supplies one photon and only a single photon at well specified time intervals. Streams of single photons can be produced in many different physical processes including nonlinear optical processes in bulk crystal [17] and in optical waveguides [18], lasing and quantum dot emissions [19]. The generation of photons in these various manners can be either deterministic or probabilistic [13]. The probabilistic methods can introduce unwanted noise to the single photon stream by generating more than one photon at a time with some non-zero probability. Often in the nonlinear processes the generation of a single photon stream begins with the production of correlated photon pairs, *i.e.*, entangled photons. The pairs are split and the detection of one of the photons in the pair indicates the existence of (heralds) the other photon. Dexterity in single photon generation and entangled photon pair generation presents a desirable platform for the quantum mechanical bussing of information.

Single photons are attractive for quantum cryptography protocols because they offer a system in which no eavesdropper can gain information [20]. Additionally, a

stream of single photons incident on a beamsplitter provides a truly random sequence in either one of the output ports of the beamsplitter. A wide variety of other applications exist ranging from biophotonics and medicine [21–24] to LIDAR and other quantum-enabled metrology techniques [25, 26].

1.2 Why use optical fibers?

Experimental optical nonlinearity in crystals was first demonstrated as second harmonic generation by Franken *et al.* in 1961 soon after the advent of the ruby laser [27]. Many research groups in the United States and the Soviet Union followed with experimental demonstrations of processes such as sum frequency generation [28, 29], third harmonic generation [30] and stimulated Raman scattering [31, 32]. These efforts resulted in a variety of tunable light sources that paved the way for numerous spectroscopic applications, e.g. multiphoton microsopy [33, 34] and squeezed light spectroscopy [35].

Optical fibers have notable nonlinearity properties which have been of interest since the 1970s [36, 37]. Fiber nonlinearity in optical communications, the largest implementation of optical fibers, is usually considered to be deleterious. However, a key advantage to utilizing optical fiber for nonlinear devices is the long interaction length and compact footprint over which nonlinear effects can occur. Another advantage inherent to fibers is their low cost and light weight. Fiber-based nonlinear technologies are especially attractive for portable, affordable, turnkey devices. This dissertation focuses on the application of third order nonlinearity in fibers to optical parametric oscillators (OPOs) which are bright, tunable laser-like light sources.

The long interaction length in optical fibers, which is advantageous for pushing the boundaries of nonlinearity, necessitates the fine control of dispersion. This is because phase-matching and group-velocity matching are critical for appreciable nonlinear effects to take place. Luckily scientists and engineers have access to the dispersion profile of fibers through manipulation of material and index variation. So called dispersion shifted fibers have a special shape in their doping profile, triangular, trapezoidal, Gaussian or otherwise, that contributes to an overall shift in the zero

dispersion wavelength [38]. Tapering of fibers is another way to adjust the dispersion in optical fibers [39]. In microstructure optical fiber, the dispersion profile is tailorable through modification of the microstructure itself [40]. The details of dispersion modification through microstructure design are further explained in chapter 3.

Generation of photons of interest in fiber is advantageous for efficient coupling between elements in an optical system [41]. The ability to guide light efficiently in a single mode over a vast spectrum in optical fiber leads to efficient collection and overall better management of the output of nonlinear optical devices. Furthermore, the nonlinear frequency conversion processes in fiber achieve similar efficiencies to that in crystal based platforms [18].

1.3 Summary of Dissertation

This dissertation focuses on the application of parametric amplification in microstructure optical fiber (MOF) to biophotonics and entangled photon pair generation. Chapter 2 provides a brief background of fiber nonlinearities as it pertains to parametric devices including a description of the physical principles of four wave mixing and the basic construction of a fiber optical parametric oscillator (FOPO). Chapter 3 presents research techniques and results on measuring dispersion in highly-nonlinear soft glass microstructure optical fibers. Challenges and unique aspects of our approach are detailed. Chapter 4 motivates the application of FOPO technology to coherent anti-Stokes Raman scattering (CARS) microscopy. Here we present research results on power maximization by exploiting the polarization dynamics in a FOPO and intensity noise characteristics of a FOPO optimized for applications to CARS microscopy. The intensity noise results include a comparison to a competitive fiber based continuum source. This comparison highlights the potential to further improve the advantages of fiber implementation in CARS systems. Chapter 5 presents a background and explanation of potential characterization experiments for a MOF source for entangled photon pairs. We present the basic principles of a fiber-based source for nonclassical light followed by some preliminary data for characterization of such a

light source. Chapter 6 summarily presents the key achievements in this dissertation and future prospects for research in this area.

Chapter 2

Fiber based parametric devices

2.1 Microstructure optical fibers

Microstructure optical fiber, also referred to as photonic crystal fiber, is a long cylindrical waveguide that guides based on a refractive index difference between air, $n_{air} = 1.00$, and silica glass, $n_{silica} = 1.46$. The holes provide a gradual effective index variation in the radial direction from the core center and can guide light with a modified total internal reflection. The microstructure features can vary greatly but a typical hexagonal lattice structure is shown in figure 2.1. The MOF parameters of interest are the hole diameter, d, and the center-to-center spacing, Λ. These parameters can be tuned to modify the average index in the holey region which creates an index contrast between the core and the holey region. Because the guiding properties are based on the interplay between the size of the microstructure features and the wavelength of the light, a wide variety of customizations can be made by adjusting these feature sizes and shapes.

Microstructure optical fiber fabrication

The typical method for manufacturing microstructure optical fiber (MOF) was first proposed in 1995 [43] wherein silica glass capillary tubes are stacked together to form a hexagonal lattice shape preform then carefully drawn down to small fraction of its original size in a draw tower. The features of the lattice are typically micron-size,

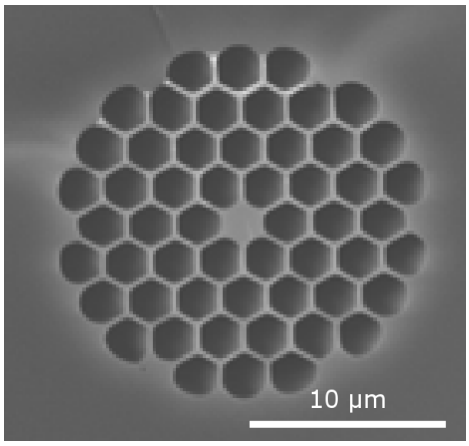

Figure 2.1: (a) An image of typical hex MOF cross-section [42].

which is on the order of the wavelength of light causing efficient scattering. The MOFs described in this dissertation have a solid silica glass core and light is guided in the core by modified total internal reflection. Here the air holes provide a gradual contrast in refractive index which defines the core-cladding edge.

An example preform is shown in figure 2.2. The preform is drawn down, sometimes in multiple steps, to a diameter on the order of a few hundred micrometers. The critical features of the structure, hole spacing Λ and hole diameter d, will be determined by the size of the small packing tubes and through control of the relative pressure in the interstitial regions and the regions within the capillary tubes. An example of the final microstructure is shown in figure 2.2.

Endlessly single mode

One attractive property of microstructure fibers is the ability to guide light in a single mode for all wavelengths for which the glass is transparent. Essentially this is possible through the difference in the way light of different wavelengths experiences the core-cladding boundary. This boundary extends deeper into the microstructure away from the axis of the fiber for light of longer wavelengths and light of shorter wavelength is confined closer to this axis. Because this adapting core-cladding boundary effect arises from the microstructure patterning it is not achievable in conventional optical fibers.

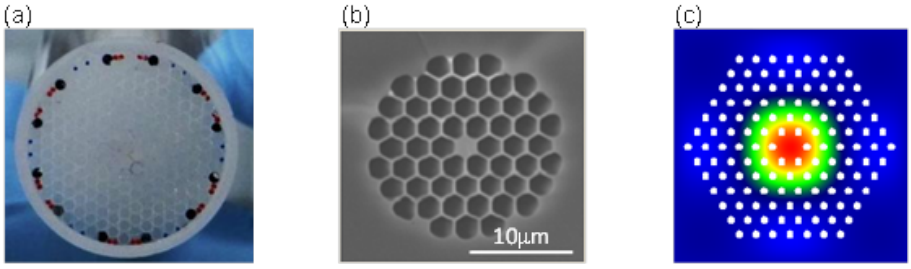

Figure 2.2: (a) An example of a microstructure optical fiber preform (left) (b) An example of the final microstructure (right) after the drawdown process Note: The MOF here(obtained from ref. [42]) is not created from the pictured preform (obtained from LLNL). Picture of the proposed fiber microstructure and fundamental mode field.

An effective V parameter, a quantity that defines the number of modes supported in an optical fiber, can be defined for microstructure fiber as

$$V_{eff} = \frac{2\pi\Lambda}{\lambda}(n_0^2 - n_{eff}^2)^{1/2} \tag{2.1}$$

where Λ is the pitch or center-to-center distance of the holes in the microstructure, n_0 is the refractive index of the glass and n_{eff} is the effective index caused by the propagation in both glass and air creating a cladding boundary. The effective index in microstructure fibers decreases at shorter wavelengths so that n_{eff} approaches n_0. This serves to cancel the $1/\lambda$ dependence of V_{eff}, making it a bounded value. In conventional solid core fibers the single mode condition is defined as $V < 2.405$ [44]. In the microstructure fibers there exists a ratio of the air hole size, d, to the pitch, Λ, in which $V_{eff} < 2.405$ for all wavelengths, thus it can be single mode at all wavelengths.

2.1.1 Soft glass microstructure optical fibers

Conventional solid-core optical fibers for communications are made of germanium doped high-purity silica glass because absorption in the telecommunications region near 1.55um can be very low at 0.2 dB/km in this material [40]. Germanium doping serves to generate an index contrast and thus defines the core-cladding boundary. In contrast, the microstructure optical fibers are typically undoped but made from the

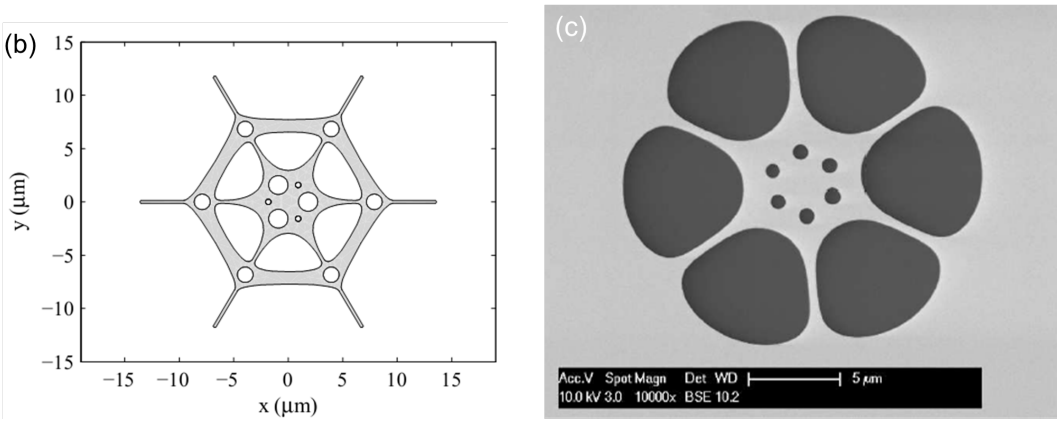

Figure 2.3: (a) A drawing depicting a complicated fiber core microstructure designed with a genetic algorithm [46]. (b) SEM image of the actual fabricated core displaying significant divergence from the intended structure.

same high-purity, low-loss silica glass. Silica glass was likely chosen for its low-loss characteristics, low cost and the existence of standard fabrication practices based on its routine use for telecommunications. However, MOFs need not be made with this material and their utility may be increased by using a different material. For nonlinear optical applications a material with higher intrinsic nonlinearity would be desirable. Nonsilica glasses exhibit a relatively greater nonlinearity and can be developed into microstructure optical fibers in the same way as the silica MOFs. Additionally, they can transmit light further into the IR range than silica glass, opening up nonlinear fiber optics to the region beyond 2um.

These nonsilica glasses are often referred to as soft glasses because of their relatively lower melting point. Handling these glasses is often nontrivial and forming complex microstructures can be difficult. In figure 2.3 the image shows a desired microstructure determined by a genetic algorithm [45]. The image in figure 2.3 shows the actual microstructure fabricated with the aim of producing the desired structure. The obvious differences here highlight the difficulty of working with these soft glass fibers.

Transmission beyond 2 m and high intrinsic nonlinearity

An Editorial in Nature Photonics from July 2012 states "The mid-infrared spectral region of 2-20 μm contains strong characteristic vibrational transitions of many important molecules as well as two atmospheric transmission windows of 3-5 μm and 8-13 μm, which makes it crucial for applications in spectroscopy, materials processing, chemical and biomolecular sensing, security and industry. [47]." Low phonon energy in the mid-IR allows some soft glasses to exhibit an extended transmission window. This class of soft glass fibers contain heavy metals such as TeO2 or GeO2, or have low bond strength such as ZrF4 and As2S3. The IR cutoff wavelength is determined by the prevalence of multiphonon absorption that arises from fundamental network vibrations. Because these vibrations are lower in some of the soft glasses their IR cutoff wavelength is shifted longer so they can efficiently transmit light in the region far beyond 2 μm unlike conventional silica glass [40]. The soft glass fibers thus present a unique platform for delivering light at these wavelengths. It is important to note that the presence of OH absorption in the mid-IR is a challenge in these fibers as well as in silica glass fibers so minimizing the atmospheric water content aids in maximizing transmission in this spectral region.

Another property of interest in the soft glasses is the high intrinsic nonlinearity in the material itself. The nonlinear parameter γ in fibers is expressed as

$$\gamma = \frac{2\pi n_2}{\lambda A_{eff}} \tag{2.2}$$

where n_2 is the nonlinear refractive index, λ is the wavelength and A_{eff} is the effective mode area (core size) [48]. This shows that the nonlinearity is inversely proportional to the core size and directly proportional to the nonlinearity of the material itself. In microstructure fibers it is possible to confine the field to a very small mode area making the nonlinearity higher through greater light-material interaction. Exploiting both material an microstructure allows for tailoring of the nonlinearity over five orders of magnitude, a much greater range than in conventional silica optical fibers where the typical nonlinear parameter is $\gamma \approx 1[W \cdot km]^{-1}$ and the maximum achievable nonlinear parameter from tailoring the microstructure is $\gamma \approx 70[W \cdot km]^{-1}$ [40]. By

utilizing a glass of high intrinsic nonlinearity the overall fiber nonlinearity is increased beyond that which is achievable by the tight confinement in the microstructure. Also the losses increase as the core size becomes smaller so a trade off exists between the nonlinear parameter and the losses due to minimizing A_{eff}. Many variations in fiber designs are being explored to push the envelope of achievable nonlinearity while maintaining practicality of fiber fabrication and implementation [45, 46, 49].

2.2 Nonlinear response

Oftentimes scientists and engineers make no fuss about nonlinearities in their experiments or models. The nonlinear optical response becomes appreciable only for cases of intense light beams in a material. In this case the driving forces on an atom or molecule in some material are intense enough such that the system responds to higher orders of the electric field. A question one might have is what might the magnitude of the electric field be when nonlinearities are considerable? Assuming that the lowest order correction to the material response is comparable to the linear response when the amplitude of the applied field is on the order of the characteristic atomic electric field strength

$$E_{atomic} = \frac{e}{4\pi\epsilon_0 a_0^2} = 5.14 \times 10^{11} V/m \tag{2.3}$$

where ϵ_0 is the permitivity of free space and a_0 is the Bohr radius of the Hydrogen atom. So the second order response might be $1/E_{atomic} = 1.94\times10^{-12} m/V$. This value is in fact reasonable compared to measured values of the second order susceptibility in condensed matter which are generally on the order of $10^{-12} m/V$ [50].

When an electromagnetic wave with field strength above this threshold propagates through transparent material, the response becomes nonlinear. Specifically the material response is the deformation of the electron cloud surrounding the nuclei of the atoms composing the material, known at the individual atom level as the induced dipole moment. Under modest field strengths, this deformation follows the electric

field linearly. To diverge from the linear regime means that the cloud deformation follows higher orders of the electric field [50]. In this case, the oscillation of the electron cloud produces radiation at frequencies other than the input.

The aggregate response in the material is described as a wave of deformation or polarization of the atoms. The induced polarization can then be generally expressed as

$$P(t) = \epsilon_0[\chi^{(1)}E(t) + \chi^{(2)}E^2(t) + \chi^{(3)}E^3(t) + ...] \tag{2.4}$$

where t is time, ϵ_0 is again the permitivity of free space and χ is a constant of proportionality called the susceptibility. The nonlinear polarization of the material can lead to the shifting of energy from the frequency of the input field to new frequencies. The simplest demonstration of this is second harmonic generation where energy can shift from the applied field frequency, ω, to the second harmonic of that frequency, 2ω, through the second order response of the material. The input field can be written

$$E(t) = Ee^{-i\omega t} + c.c. \tag{2.5}$$

where ω frequency of the electric field, E is the amplitude and c.c. is the complex conjugate. The second order term of the induced polarization can be written in term of this expression for the electric field

$$P^{(2)}(t) = 2\epsilon_0\chi^{(2)}EE^* + (\epsilon_0\chi^{(2)}E^2e^{-i2\omega t} + c.c.) \tag{2.6}$$

where now it can be seen that the second order material polarization consists of a contribution at twice the input frequency, 2ω. The oscillation of the dipoles at the frequency then generates radiation at 2ω a new frequency component to the field. This is fittingly referred to as "frequency doubling or formally, second harmonic generation. Note that the first term in this expression has no frequency dependence, in fact it produces a static field across the medium and it is referred to as optical rectification.

2.3 Parametric Amplification and Four Wave Mixing

Nonlinear optical processes in optical fibers are those where the material actively participates in the modulation process or it can passively participate. In stimulated Raman scattering the molecular vibrations play an active role in the optical frequency shifting process. In stimulated Brillouin scattering the density variations along the light guiding path serve actively in the process as well. In contrast there are so called parametric processes wherein the material itself is unchanged in the process. Here there is a passive modulation of the material parameters.

The dominant parametric process in optical fibers is four wave mixing. Four wave mixing is a third order nonlinear optical process that experiences appreciable gain in silica, an isotropic medium. Third order processes involve the interactions between four optical waves. Dropping the time dependence from the previous section, the induced nonlinear polarization in the third order is given by

$$P_{NL} = \epsilon_o \chi^{(3)} |E|^3 \tag{2.7}$$

let the electric field, E, be expressed as

$$E = \frac{1}{2}\hat{a}\sum_{j=1}^{4} E_j e^{i(\beta_j z - \omega_j t)} + c.c.) \tag{2.8}$$

where the index $j = 1, 2, 3, 4$ represents the four optical waves, ω_j is frequency, z is the spatial coordinate along the length of the fiber and βj is the propagation constant. The induced nonlinear polarization can then be rewritten in the form

$$P_{NL} = \frac{1}{2}\hat{a}\sum_{j=1}^{4} P_j e^{i(\beta_j z - \omega_j t)} + c.c.) \tag{2.9}$$

where the nonlinear induced polarization,P_{NL}, is now written as a function of the linear induced polarization, P_j. P_j for $j = 1, 2, 3, 4$ involves many terms of the products of three electric fields. Active terms are governed by minimizing the phase

mismatch between E_4 and P_4. Both the phases and the wave vectors between the optical fields must match. The matching of frequencies is intrinsically tied to the chromatic dispersion in the material and the matching of wave vectors is related to the group velocity dispersion. Thus the choice of input frequency and dispersion parameters is critical to achieve high efficiency in the four wave mixing process.

Considering the case where pumping is degenerate and undepleted, phase matching and group velocity matching require the following conditions

$$\omega_3 + \omega_4 = \omega_1 + \omega_2 \tag{2.10}$$

and

$$\Delta k = \beta_3 + \beta_4 - \beta_1 - \beta_2 = 0 \tag{2.11}$$

where $\omega_{1,2}$ represent the pump frequency and ω_3 and ω_4 are called the signal and idler frequencies, scattered symmetrically in spectrum about the pump frequency and $\beta = \tilde{n}\omega/c$ where $\tilde{n}$ is the effective mode index at the frequency ω and c is the speed of light. Here the requirement that wave-vector mismatch Δk be minimized is basically a statement of the phase-matching requirement. The frequency shift if signal and idler away from the pump, Ω_s, follows the relation

$$\Omega_s = \omega_1 - \omega_3 = \omega_4 - \omega_1 \tag{2.12}$$

The gain experienced in all four fields as a function of length along the fiber is described with four coupled amplitude equations.

$$\frac{dA_1}{dz} = \frac{in_2\omega_1}{c}\left[(f_{11}|A_1|^2 + 2\sum_{k\neq 1} f_{1k}|A_k|^2)A_1 + 2f_{1234}A_2^* A_3 A_4 e^{i\Delta kz}\right] \tag{2.13}$$

$$\frac{dA_2}{dz} = \frac{in_2\omega_2}{c}\left[(f_{22}|A_2|^2 + 2\sum_{k\neq 2} f_{2k}|A_k|^2)A_2 + 2f_{2134}A_1^* A_3 A_4 e^{i\Delta kz}\right] \tag{2.14}$$

$$\frac{dA_3}{dz} = \frac{in_2\omega_3}{c}\left[(f_{33}|A_3|^2 + 2\sum_{k\neq 3} f_{3k}|A_k|^2)A_3 + 2f_{3412}A_1A_2A_4^* e^{-i\Delta kz}\right] \tag{2.15}$$

$$\frac{dA_4}{dz} = \frac{in_2\omega_4}{c}\left[(f_{44}|A_4|^2 + 2\sum_{k\neq 4} f_{4k}|A_k|^2)A_4 + 2f_{4312}A_1A_2A_3^* e^{-i\Delta kz}\right] \tag{2.16}$$

where A is the amplitude of the electric field, the overlap integral is given by

$$f_{ijkl} = \frac{< F_i^* F_j^* F_k F_l >}{[< |F_i|^2 >< |F_j|^2 >< |F_k|^2 >< |F_l|^2 >]^{1/2}} \tag{2.17}$$

where F is a function of the transverse coordinates x and y and describes the transverse distribution of the fiber mode i, j, k or l. Here the angle brackets indicate integration over transverse coordinates x and y. Assuming all fields are continuous wave and single mode

$$f_{ijkl} \approx f_{ij} \approx \frac{1}{A_{eff}} \tag{2.18}$$

the solutions are found numerically. The first two of the four coupled amplitude equations are solved to obtain

$$A_1(z) = \sqrt{P_1}e^{i\gamma(P_1+2P_2)z} \tag{2.19}$$

$$A_2(z) = \sqrt{P_2}e^{i\gamma(P_2+2P_1)z} \tag{2.20}$$

where

$$\gamma_j = \frac{n_2\omega_j}{cA_{eff}} \approx \gamma \tag{2.21}$$

$$P_j = |A_j(0)|^2 \tag{2.22}$$

where P_1 and P_2 are incident pump powers at z=0.

These solutions are then substituted into the other two equations of the four coupled amplitude equations to get

$$\frac{dA_3}{dz} = 2i\gamma\big[(P_1 + P_2)A_3 + \sqrt{P_1P_2}e^{i\theta}A_4^*\big] \tag{2.23}$$

$$\frac{dA_4^*}{dz} = -2i\gamma\big[(P_1 + P_2)A_4^* + \sqrt{P_1P_2}e^{i\theta}A_3\big] \tag{2.24}$$

where

$$\theta = [\Delta k - 3\gamma(P_1 + P_2)]z \tag{2.25}$$

Introducing a change of variable, $B_j = A_j e^{-2i\gamma(P_1+P_2)z}$ where $j = 3, 4$, the equations become

$$\frac{dB_3}{dz} = 2i\gamma\sqrt{P_1P_2}e^{-i(\kappa z)B_4^*} \tag{2.26}$$

and

$$\frac{dB_4^*}{dz} = 2i\gamma\sqrt{P_1P_2}e^{i(\kappa z)B_3} \tag{2.27}$$

where $\kappa = \Delta k + \gamma(P_1 + P_2)$ represents the effective phase mismatch.

The solutions are

$$B_3(z) = (a_3e^{gz} + b_3e^{gz})e^{-i\kappa z/2} \tag{2.28}$$

and

$$B_4^*(z) = (a_4e^{gz} + b_4e^{gz})e^{i\kappa z/2} \tag{2.29}$$

where

$$g = \sqrt{(2\gamma P_1P_2) - (\kappa/2)^2} \tag{2.30}$$

is known as the parametric gain and the constants a_3, a_4, b_3 and b_4 are determined from the boundary conditions.

In the degenerate case, $P_1 = P_2 = \frac{P_0}{2}$ and $\kappa = \Delta k + 2\gamma P_0$. From this it is evident that the gain, g, will change as Δk changes and the maximum gain g_{max} occurs when $\Delta k = 0$ or $-2\gamma P_0$. This is basically a statement of the phase matching requirement for appreciable four wave mixing gain. In this case a continuous wave input was considered allowing for group velocity dispersion effects to be ignored. If the input is a pulsed source, the group velocity dispersion is considered by allowing the amplitude, $A_j(z)$, to be a slowly varying function of time. The overall effect of this for a given amplitude equation is that it becomes a partial differential equation of the length coordinate, z, and time, t, with a term containing β_2 as in

$$\frac{dA_j}{dz} \rightarrow \frac{\delta A_j}{\delta z} + \beta_{1j}\frac{\delta A_j}{\delta t} + \frac{i}{2}\beta_{2j}\frac{\delta^2 A_j}{\delta t^2} + \frac{1}{2}\alpha_j A_j \tag{2.31}$$

It is important to note that the group velocity dispersion can be very different for the four pulses involved so the group velocity matching is important in order to achieve nearly maximum gain.

The effective phase mismatch, κ, can be rewritten as the phase matching terms from from the linear and nonlinear effects in the fiber

$$\kappa = \Delta k_M + \Delta k_{WG} + \Delta k_{NL} = 0 \tag{2.32}$$

where Δk_M is the contribution from the material dispersion, Δk_{WG} is the contribution from the waveguide dispersion and Δk_{NL} is the contribution from nonlinear effects. In single mode fiber Δk_{WG} will be equal to zero provided that all four fields are guided in the single mode regime. The effective phase mismatch is then minimized through the interplay of material dispersion and nonlinear effects. It is evident that one of these parameters must be negative in order to phase match the effect. Phase matching is generally achieved by placing the pump frequency slightly in the anomalous dispersion regime so that the material dispersion Δk_M becomes the negative value but this can also be achieved through tuning the nonlinearity with the pumping power or by exploiting birefringent properties in the fiber. Pumping with a modest power at a

frequency near the zero dispersion frequency ensures that the system is in a low Δk_M and low Δk_{NL} regime where four wave mixing gain will be appreciable.

Gain in new spectral components is the final result. If the a weak field in the gain spectrum (signal) is injected along with the pump, the amplification factor for this weak field will be

$$G_{sig} = P_{sig}(L)/P_{sig}(0) = 1 + (\gamma P_0/g)^2 \sinh^2(gL) \tag{2.33}$$

where $P_{sig}(L)$ is the power in the signal field at a length L along the fiber and $P_{sig}(0)$ is the power in the signal field at the input of the fiber. The system is working as an amplifier if this ratio is greater than one. Notice that this expression on the far right is a function of the parametric gain defined in equation 2.30. Additionally, it is a $\sinh^2$ function of L which is ever increasing. This is not realistic and it results from assuming no depletion of the pump and ignoring saturation effects. These new field components are usable as broadband and tunable laser-like light.

2.4 Fiber Optical Parametric Oscillators

Parametric gain in fibers or crystals can be used to amplify a weak field within the gain spectrum of the parametric process involved. The amplification can be supported further with oscillation much like that in a laser cavity. Here the weak field from a signal or idler frequency can be injected into the system from a second pumping source or the spontaneous fields created from the parametric process itself can be fed back into the system. The system can be resonant with one or both of the sidebands. A typical fiber optical parametric oscillator system is depicted in figure 2.4 and bears similarity to a typical solid state laser system with the gain medium replaced by a highly nonlinear optical fiber.

In the fiber optical parametric oscillators (FOPOs) four wave mixing is the parametric process that serves to convert input light frequency. On a single pass through the fiber, spontaneous four wave mixing promotes gain in the sidebands. By placing a cavity around the gain fiber that is resonant with one or both of the sidebands

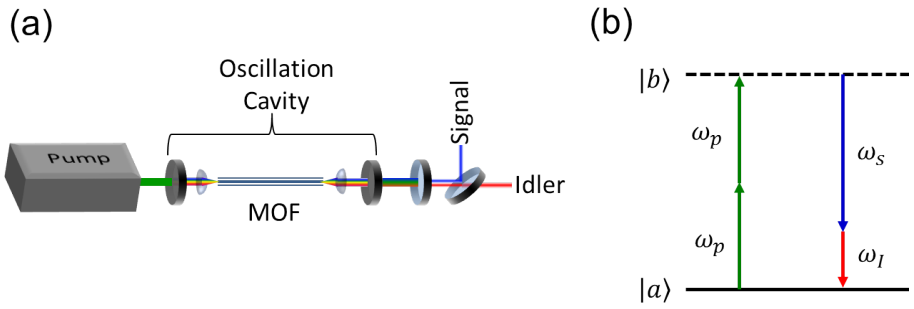

Figure 2.4: (a) Schematic of a typical fiber optical parametric oscillator setup based on a microstructure optical fiber (MOF) as the gain medium. (b) Quantum mechanical representation of the photon frequency conversion in the four wave mixing process.

the stimulated four wave mixing process can be promoted. The stimulated process narrows the spectrum and further amplifies the sidebands. This can be observed in the spectrum shown in figure 2.5

The cavity length is set to synchronously pump the OPO meaning that the round trip time of pulses in the cavity is matched to the period of the pump laser repetition rate. This ensures that the fed back pulses re-enter the fiber input at the same time that a new pump pulse enters. The overlap of these pulses in space and time maximizes the gain in the signal and idler sidebands.

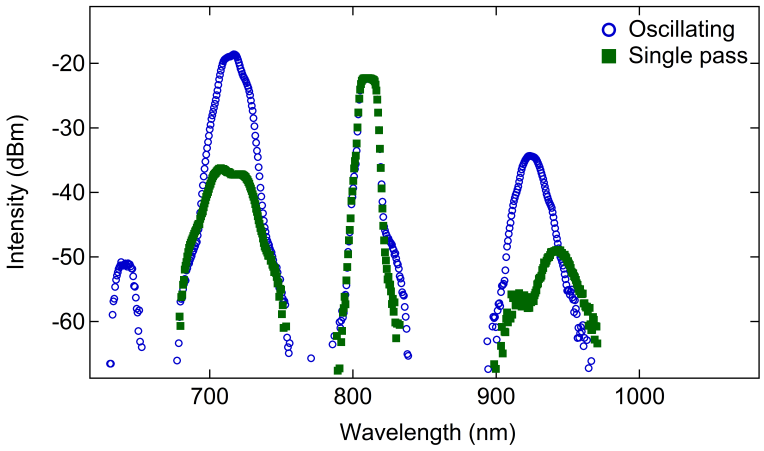

Figure 2.5: Plot of the output of a fiber optical parametric oscillator pumped at 810 nm by a tunable Ti:Sapph with pulses on the order of picoseconds. The blue curve represents the output of the device when the sidebands are allowed to oscillate in the cavity while the green curve shows the output when the cavity is blocked which is the single-pass spontaneous amplification. Notice that the sidebands of the oscillating output are about 20 dB greater in intensity and visibly narrower in spectrum.

Chapter 3

Dispersion in soft glass microstructure fibers

A simple dispersion measurement becomes troublesome in highly nonlinear optical fibers. Dispersion is a linear optical phenonmenon and the high nonlinearity in these fibers can influence the measurement by introducing effects from the nonlinear refractive index, n_2. As explained in the previous chapter, nonlinear effects are stimulated when the optical field strength is large enough to perturb the material polarization nonlinearly. Practically speaking, in the pulsed light sources we use, the field strength is related to the optical power or pulse duration. Controlling these input parameters offers some reduction in the nonlinear effects but the tunable sources available to us are generally nonlinear devices themselves; they are high power with short pulses. In this chapter, we show the details and explain some of the challenges in a dispersion measurement on a soft glass microstructure optical fiber.

3.1 Dispersion tailoring

For nonlinear optical applications in microstructure fibers, it is essential to be able to generate a suite of properties in the fiber by defining the glass type and the microstructure. High nonlinearity, low-loss and fine control over dispersion are the primary properties that a fabricator is interested in designing. High nonlinearity is

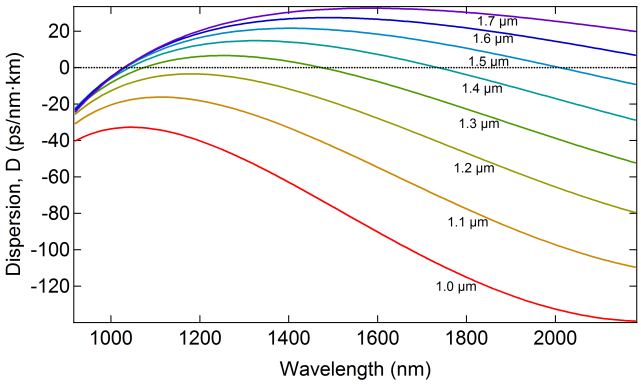

Figure 3.1: Shows the calculated dispersion parameter, D, for a microstructure optical fiber modeled as a glass rod in air. Curves are plotted as a function of wavelength for various core sizes ranging from 1.0 μm to 1.7 μm pumped from 910 nm to 2190 nm. The various core sizes, controlled by the microstructure design, shift the zero dispersion wavelength. The zeros of the dispersion curve are advantageous pumping regions to stimulate phase matching in four wave mixing.

achieved in MOFs by creating a tight mode confinement with a small core size which generally increases the effects of light-material interactions [49]. Simultaneously, the dispersion and losses need to be managed by controlling the glass-air ratio.

As shown in figure 3.1, the MOF dispersion parameter can shift a great deal with a relatively small change in the glass-air ratio so the overall dispersion can vary greatly from the dispersion of the glass composition [51]. Figure 3.1 shows a calculation of dispersion parameter, D, for a MOF modeled as a glass rod suspended in air. It shows that the zero dispersion wavelength (ZDW) can be shifted by changes in the microstructure that change the core size of the fiber. The ability to control the ZDW of these fibers is essential for FOPO operation in many regions of spectrum. An ideal fiber for dramatic nonlinear effects would have high nonlinearity and low dispersion in the pumping region. Since small changes in the microstructure can result in such varied dispersion profiles [49], the potential for various MOF and pump laser combinations is promising. However, current fabrication methods face challenges that compromise sufficient homogeneity in the microstructure for such well-defined dispersion tailoring.

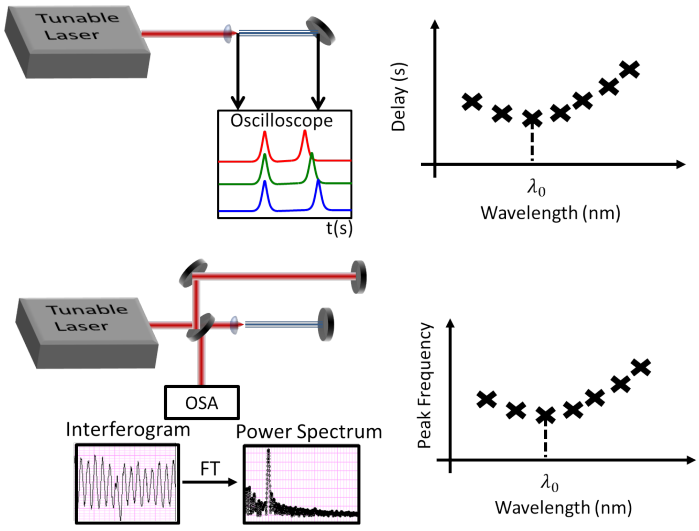

Figure 3.2: (a)Schematic of time-of-flight dispersion measurement. Tunable pulses are coupled into the test fiber, reflections from before the fiber and after the fiber are collected and sent to a fast detection oscilloscope. The temporal delay between these pulses is measured for various wavelengths. (b) Schematic of the interferometric dispersion measurement. Frequency of the fringes in the spectral interferogram varies with input wavelength. The peak locations from Fourier transform of the interferogram are plotted vs. center wavelength of the spectral window and the delay is given by calibration for a known delay.

3.2 Measuring dispersion

We show two methods to measure the fiber dispersion. The time-of-flight method is a straightforward method used for fibers exceeding one meter, where nonlinearity is modest or low [52]. For highly nonlinear fibers where fiber lengths are less than one meter there is an interferometric method of measuring dispersion [53,54]. In the time-of-flight measurement, depicted in figure 3.2(a), the relative delay of optical pulses as a function of wavelength for the fiber under test. With a sufficient range of test wavelengths, this plot will show a turning point. This turning point is an indicator of the location of the zero dispersion wavelength for this fiber, which is generally not at the same wavelength as the zero dispersion for the bulk material.

In practice it can be difficult to fabricate the exact microstructure properties

intended by engineers. Nevertheless the fiber dispersion can be estimated with confidence by modeling the core as a glass-rod. Furthermore, it can be difficult to measure the dispersion curve over a wide spectral window and the tunable source stability influences the measurement significantly. In figure 3.3 a high power tunable solid-state OPO was used to obtain 200 fs pulses tunable in the range of 1500 nm (APE PPLN crystal OPO pumped by a Coherent MIRA HP pumped by Coherent Verdi 18 W) for a dispersion measurement of 20 cm of soft glass microstructure optical fiber (SF57 Hex-Wagon Wheel). The energy of output pulses from the OPO are typically in the nanojoule range with peak powers in the kW range so injection into highly nonlinear fiber is likely to stimulate nonlinear optical processes. The injected light is attenuated to suppress broadening of the pump, an indicator of nonlinear regime, in order to ensure measurement of linear dispersion.

Additionally, it can be difficult to get light coupled into the fiber because the core size can be very small. A high numerical aperture (NA) lens is one way to maximize the coupling efficiency into the fiber. Another method we found to be effective is to first couple light into a short piece of conventional SMF-28 fiber then butt-couple the output into the soft glass MOFs. We were able to finely control the butt-coupling alignment using the motorized translation stages in an optical fiber splicer (Fujikura 40 S). A coupling ratio of about 25 % was typical with this method.

3.3 Nonlinear effects

Difficulties in measuring the dispersion arise from the high nonlinearity. The influence of the nonlinear refractive index, n_2 becomes considerable for sufficient peak power pulses. A practical indicator of the high nonlinearity regime is spectral broadening due to self phase modulation. We observed this broadening in two soft glass MOFs, SF57 Hex Wagon-Wheel (SF57 HWW) and Bismuth doped Hexagonal Wagon-Wheel (Bis HWW). Three plots of pump broadening in 20 cm of SF57 HWW are shown in figure 3.4. The pump wavelength and pumping power are varied with the goal of observing degenerate four wave mixing when the fiber is pumped close to the zero dispersion wavelength. The pump wavelengths are 1600 nm, 1650 nm and 1675 nm. In figure

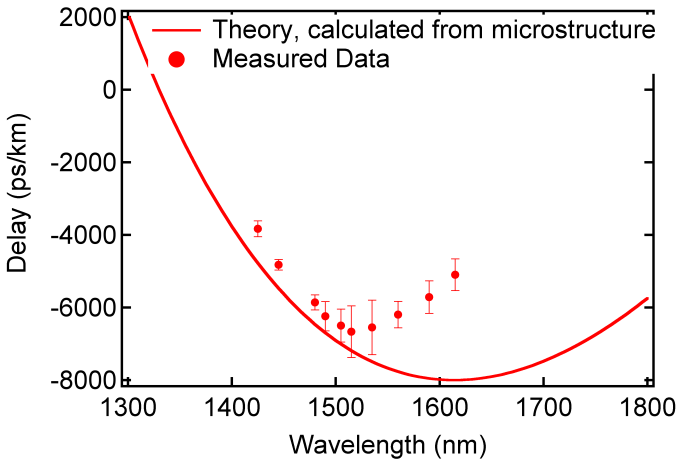

Figure 3.3: Measurement of delay (ps) as a function of via Fourier transform spectral interferometry (FTSI) of SF57 Hexagonal wagon-wheel microstructure optical fiber. The solid line represents a theoretical calculation of the delay from the fiber material and microstructure. The points represent measured delay.

3.4(a) modest broadening for three different pumping powers is evident. Broadening here is due to self phase modulation of the pump at 1600 nm, which is likely to be in the normal dispersion (known from theoretical calculation). Figure 3.4(b) shows pronounced broadening and perhaps the emerging of new peaks as the input power is increased is a sign of four wave mixing but it is difficult to decouple that effect from the self phase modulation broadening. Figure 3.4(c) shows broadening but no clear signs of four wave mixing. Assuming this pronounced broadening is from noisy four wave mixing, this result is some indication that the zero dispersion wavelength is located near 1650 nm.

One practical difficultly in the mid-IR region is the accessibility of tunable light sources and detectors in that region. As explained in section 2.1.1, scientists are interested in generating parametric amplification in the spectral region past 2μm. This is possible with four wave mixing in soft glass MOF because the zero dispersion wavelength can be shifted further into the IR and the transmission window can extend far into the IR as well. However, the characterization experiments were challenging because light sources and detectors available at the time of this study did not extend into this range of spectrum. It is important to note that detectors do exist for

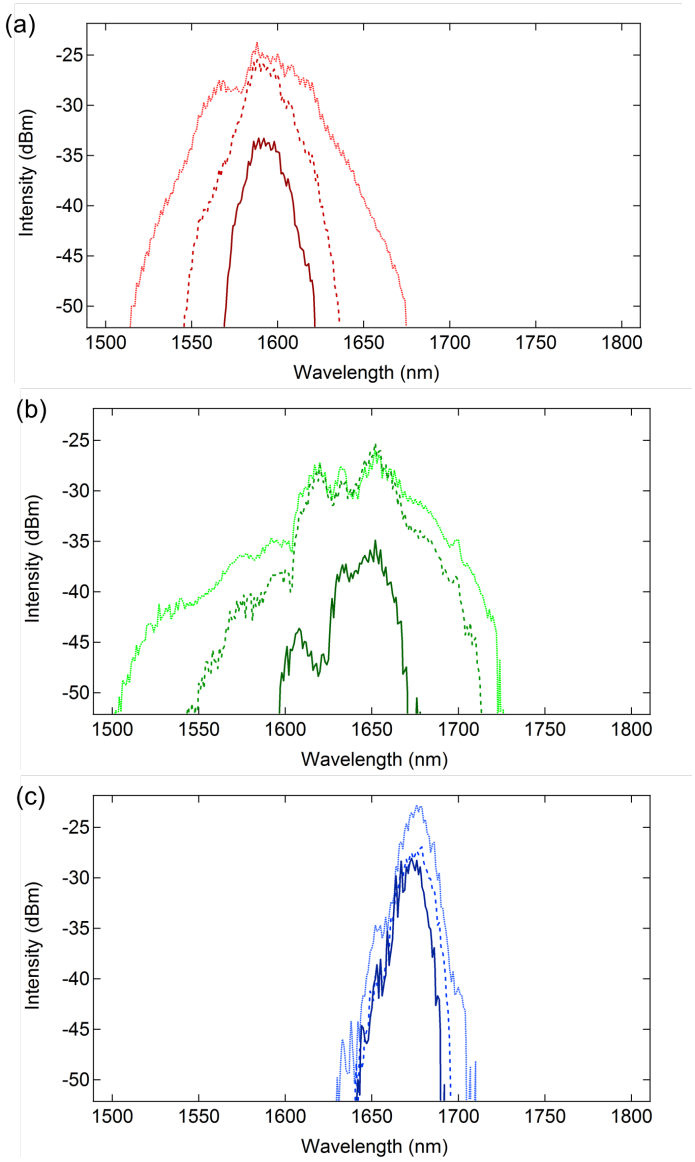

Figure 3.4: Plots of broadening due to self phase modulation in 20 cm of SF57 HWW soft glass microstructure optical fiber. Pumping power is increased for three different pumping wavelengths (a) 1600 nm (b) 1650 nm and (c) 1675 nm. Pronounced broadening and multiple peaks that emerge for large pumping powers in plot (b) indicates that the zero dispersion wavelength near 1650 nm.

detection well past 2μm, for example deuterated triglycine sulfate (DTGS) detectors or HgCdTe detectors.

We show an attempt to inject pulses of longer wavelengths by generating Raman shifted solitons in a long piece (about 500 m) of SMF-28 fiber. The amount of red shifting was controlled by attenuation at the input of the fiber. More injected power cause the soliton to be shifted to longer wavelengths. The solitons were then used to pump a section of the highly nonlinear soft glass MOFs. The nonlinear gain spectrum was recorded as a function of the soliton wavelength with the expectation that nonlinear gain, specifically the four wave mixing gain, would indicate an approximate zero dispersion wavelength. Resulting spectra were difficult to interpret because the interference of many nonlinear effects was likely increased from the highly compressed, and thus high peak power, characteristic of soliton pulses. In fact the generation of dispersive waves was observed in 20 cm of SF57 fiber which is indicative of soliton breakup, a process which occurs in the regime of high nonlinearity. The red shifted peaks in figure 3.5 are the Raman shifted solitons. They shift further into the IR as the pump power increases. The blue shifted dispersive waves, seen in the range of 1300 nm to 1400 nm, are generated by the leaking of energy from these solitons, likened to Cherenkov radiation [48].

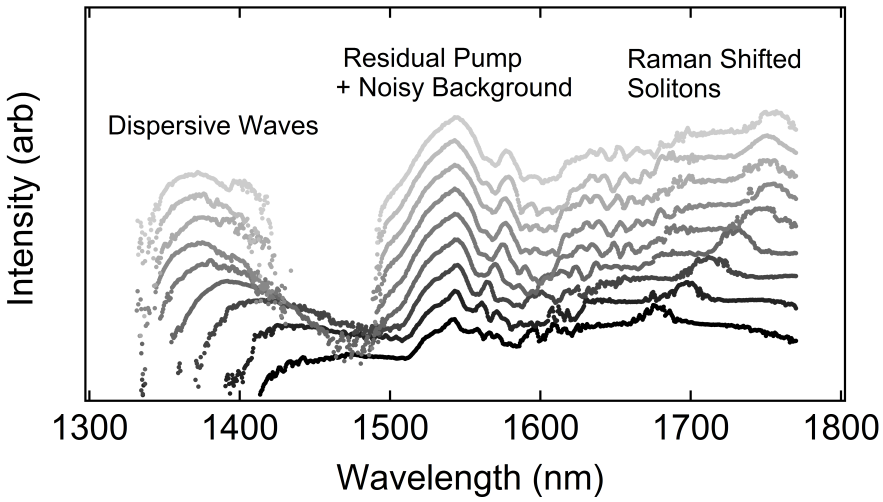

Figure 3.5: Dispersive wave generation as a function of input pumping power. Shown here are plots of the output spectrum for 20 cm of SF57 fiber pumped by a Raman shifted soliton in the range of 1700 nm. The plots are displaced vertically in order for the reader to easily see the peak growth and shifting. Traces are plotted in order of increasing input power from the bottom to the top where the maximum pumping power to the SF57 fiber is about 40 mW. Dispersive wave growth and shift in the range of 1300 nm to 1400 nm as a function of input power to the soliton.

Chapter 4

Fiber based light sources for CARS

The development of cost-effective and user-friendly ultrafast light sources is essential for increasing the impact of multiphoton microscopy. Coherent anti-Stokes Raman scattering (CARS) microscopy is of a particular interest because it allows for label-free, chemical-specific microscopy at imaging rates comparable to dynamic biological processes [10]. CARS requires two synchronized pulse trains that act as pump and a Stokes beam to coherently drive the Raman vibrational modes in a material of interest. Some coherent Raman scattering implementations use multiple synchronized optical parametric oscillators, while lower cost systems use a single ultrafast light source and continuum generated from nonlinear processes in optical fiber [10]. The most common light sources for CARS are Nd:YVO4 pumped solid-state optical parametric oscillators as in Ref. [55]. These systems are expensive and bulky compared to their fiber-based counterparts. Several groups have demonstrated the use of supercontinuum [56–58] and fiber-optical parametric devices as light sources for CARS imaging [59–61].

The ideal source parameters for CARS microscopy are the ability to supply two 1 ps long pulse trains, with at least one that is tunable in the near-IR, both at a repetition rate of 10 MHz or higher with an average power of about a Watt [10]. Two pulse trains are needed to stimulate the coherent scattering from Raman vibrations in a sample. In principle and two frequencies that have a difference that matched the Raman vibrational mode of interest can be used for CARS but laser excitations

in the near-IR have been shown to minimize the nonresonant background noise [62]. Additionally the near-IR excitation results in reduced photodamage and deeper penetration into the tissue [63]. Pulse durations are optimal in the few picosecond range in order to match the transform limited spectrum to the generally narrow, approximately 1 nm, natural linewidths of the molecular vibrations [55]. At least 10 MHz repetition rate of the pulses is necessary for video rate imaging with 10 mega pixels per second and one allotted pulse per pixel.

One approach to increasing the number of accessible Raman vibrations in a CARS measurement involves using a broadband continuum source. Fiber-based sources can meet this criteria but it is important to consider the additional noise that any source will apply to the CARS signal. Also the amount of power per spectral mode is a critical consideration in the selection of CARS light source. We have built a FOPO system tailored for CARS microscopy applications and studies of the maximum achievable output power through polarization management and intensity noise are presented in this dissertation.

4.1 Output power increase through polarization management

There have been several recent developments in FOPO design and optimization for improved performance. Xu, *et al.* designed a multi-watt FOPO based on dispersion-shifted fibers in which the output power was maximized by choosing the optimum feedback fraction for a given input pump power [64]. Murray *et al.* utilized gain-switched diodes as the seed source for a tunable FOPO system [65]. The methods used for FOPO optimization usually involve tailoring the pump source or the fiber. A recent publication by Jin *et al.* determined that the highest output powers in FOPOs are achieved with high output coupling ratios close to 1 [66]. Their study did not consider the effects of polarization in output coupling. In most FOPO implementations one extracts a large amount of energy from one sideband and minimizes loss in the remaining sideband in order to keep the FOPO above oscillation threshold [36, 67].

Here we couple out both signal and idler to increase the tunability of the system.

Motivated by the desire to tailor FOPO performance for CRS applications, we study a FOPO that: 1) is pumped by picosecond pulses; 2) has the majority of the cavity within optical fiber; and 3) has the ability to couple out energy from both sidebands with sufficient power to allow for any combination of signal, idler, and pump for CARS stimulation which maximizes the accessible Raman wave numbers. In this chapter, we present experimental results and numerical simulations for such a system. 75% of the cavity in this FOPO is within fiber and output pulse durations are 2.2 ps. The wavelength tuning range is from 960-1044 nm for the signal and 1084-1191 nm for the idler. The wavelengths for peak operation are 992 nm and 1147 nm. A significant portion (80% , 70 mW) of energy from each of the sidebands is coupled out using a polarization-based output coupler.

A FOPO operates based on four wave mixing (FWM) within an optical fiber. With sufficient FWM gain the FOPO can tolerate high losses and still be operational [66, 68]. Under these conditions, the FOPO operates where FWM dominates over other nonlinear effects such as supercontinuum generation or stimulated Raman scattering [61]. The FWM process is polarization dependent for two key reasons. Firstly, the propagation constants and thus the phase matching conditions are usually polarization dependent. Secondly, the susceptibility, χ, is a tensor quantity having different values associated with the coupling of cross-polarized fields [48]. Consequently, polarization-based output coupling schemes introduce additional complexity to what would normally be a single-polarization FWM device, requiring attention to polarization state at various positions in the cavity.

Our microstructure fiber is non-polarization maintaining. Lacking clear polarization modes makes it difficult to determine the ideal input pump polarization and, therefore, to understand the polarization dynamics within the FOPO. Nevertheless, we find experimentally that using a polarization-based output coupling scheme with this system provides essential flexibility in adjusting the output power coupling ratio while maintaining stable operation. Our simulations confirm that we obtain high output power for the case in which the polarization state of the oscillating mode within the FOPO cavity is adjusted to overlap with that of the pump polarization mode.

A schematic of the FOPO is given in Fig 1. The FOPO consists of a 1.2-m long microstructure fiber (NKT Photonics, NL-5.0-1065) pumped by a mode-locked 1064nm Nd:Vanadate laser (Time Bandwidth, 800 mW output power, 80 MHz repetition rate, 8 ps pulse duration). We couple as much as 550 mW of average pump power (800 W peak power) into the fiber. A diagram of the setup is shown in figure 4.1. Spectral broadening of pump pulses due to self-phase modulation in a single pass through the fiber indicates a nonlinear phase shift as high as 3π for our system which agrees well with the value calculated from the $\gamma PL = 10$ where γ is the fiber nonlinear coefficient, P is the peak power of the pump pulses and L is the fiber length [48]. The front cleave of the fiber and the end mirror form a Fabry-Perot cavity that is synchronous with the repetition rate of the pump laser. We chose a Fabry-Perot cavity over a ring cavity for simplicity in alignment. Wavelength tuning occurs by changing either the angle or position of the end mirror, M2, which adjusts the lowest loss wavelength in the cavity. The FOPO is tunable from 960-1044 nm on the anti-Stokes side and 1084-1191 nm on the Stokes side with output pulse durations of 2.2 ps. Additional details for a similar FOPO system are given in Ref. [67].

For this study we do not characterize every wavelength. Instead we optimize the FOPO for output power which is within a range of 994 to 991 nm for signal and 1146 to 1150 nm for idler. The state of cavity polarization state is controlled with two half-wave plates (HWP2 and HWP3) and a fiber polarization controller (FPC). Adjusting HWP2 rotates the polarization at the fiber input. Adjusting the FPC alters state of polarization traveling through the fiber. HWP2 is adjusted to maximize coupling efficiency of the pump through the fiber, we assume this polarization state is co-aligned with the fast axis of the fiber. The coupling efficiency is influenced by the input polarization because generally MOFs possess intrinsic birefringence. The FPC is also initially adjusted to maximize coupling efficiency.

In a simple reflection based output coupling scheme, the FOPO behavior traverses through three conditions as the output coupling ratio is adjusted: 1) the oscillator is well above threshold because most of the power is fed back into the cavity (relatively low loss), but the output power is minimal; 2) a large amount of energy is coupled out, but enough power remains in the cavity for efficient gain and oscillation; and 3)

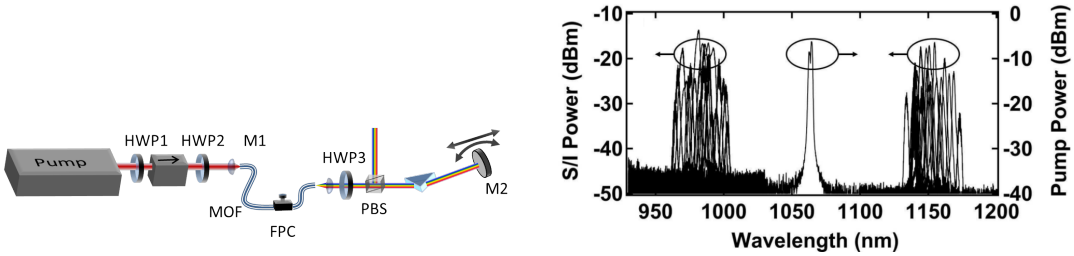

Figure 4.1: (a) Schematic of the fiber optical parametric oscillator. A Fabry-Perot cavity if formed between the input cleave of the fiber and the end mirror denoted as M2. (b) Plot of the output tuning spectrum of signal and idler sidebands. Here the cavity is tuned both by changing the cavity length and feedback angle from M2.

the output coupling fraction is so large that the power fed back into the cavity falls below oscillation threshold.

In contrast, the output coupling of all three fields in our system is polarization based. At the output of the fiber, HWP3 controls the polarization incident on the PBS which reflects s-polarized light and transmits p-polarized light. The transmitted light is reflected back into the cavity and thus adjustments to HWP3 also change the state of polarization of the field fed back into the fiber. The ability to achieve the maximum sideband output power is determined by both the output coupling ratio and the polarization overlap of the counter-propagating beams within the cavity. By adjusting only HWP3, one can optimize the output power of the FOPO by controlling the power coupled out of the system. By adjusting HWP2, FPC, and HWP3, one can optimize the output power of the FOPO by controlling both the power coupled out of the system and the polarization overlap in the fiber which contributes to the maximization of gain in the signal and idler fields.

The polarization dynamics in the cavity can be visualized on the Poincare sphere. If the polarization of the pump at the fiber output is completely p-polarized and the HWP3 fast axis is aligned with this polarization then there will be maximum transmission through the PBS; the reflection from the end mirror and the transmission back through the PBS and HWP3 will not change the polarization orientation as light is coupled back into the fiber. This is shown in figure 4.2(a). This is analogous to the simple reflection output coupling scheme. If the polarization of the pump at the

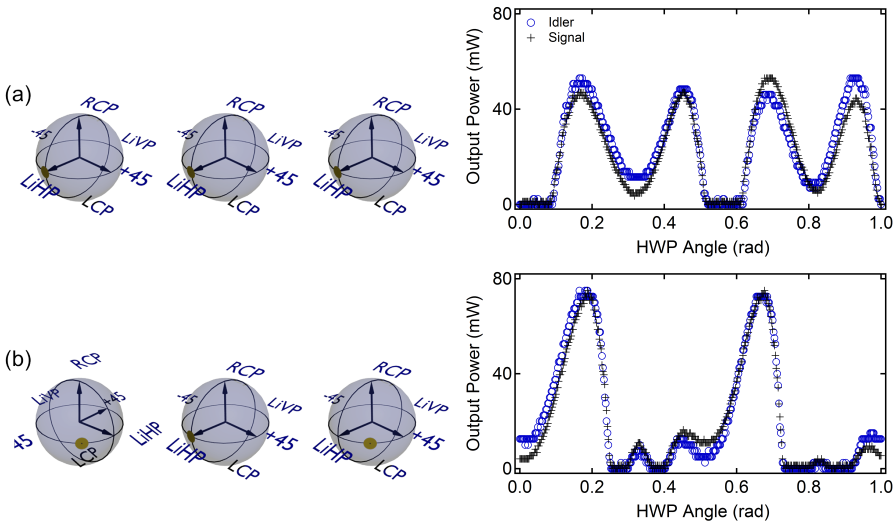

Figure 4.2: Polarization evolution at three points in the FOPO cavity: (1) input to the fiber, (2) within the cavity after the output coupler and (3) feedback into the fiber. The set of spheres in (a) represents a scenario where the polarization state remains the same (linear horizontal) throughout the cavity while (b) represents a case where the input polarization is set to a mixture of linear horizontal and linear vertical polarizations and the feedback polarization is made to overlap with the polarization of the incoming pulses. This allows for a greater maximum achievable output power. In the output waveforms as function of HWP3 rotation, we observe two unique cases: symmetric (a) and asymmetric (b).

fiber output is not completely p-polarized then the feedback polarization will not, in general, be overlapped with the fiber output polarization. HWP3 can be used to reorient the feedback polarization in order to maximize overlap without sacrificing the ability to output couple an appreciable amount of power. These scenarios are depicted as idealized (lossless) vectors on the Poincare sphere in figure 4.2. We refer to these two cases as the asymmetric and symmetric cases because of the shaping in the output traces of output power as a function of HWP3 angle.

To explore the various states of cavity feedback, we mounted HWP3 on a motorized rotating stage to rapidly measure output power based on changing polarization states at the output of the fiber. The FOPO outputs (pump, signal and idler) were recorded on an oscilloscope for waveform analysis. We observe the FOPO output waveform as we adjust the polarization state of the pump pulses propagating through

the fiber by varying FPC and HWP2. Figure 4.2 illustrates the two contrasting measurements of the output power of the FOPO as a function of waveplate (HWP3) orientation, symmetric and asymmetric.

Symmetric

In figure 4.2(a) we see that the signal and idler have essentially overlapping waveforms and each of the four peaks is roughly the same height and so figure 4.2(a) is called the symmetric condition. We observe a flat region of the curve indicating that FOPO is not operational. Here the output coupling ratio is too large and cavity losses are too high that the FOPO is below threshold. As the HWP3 angle increases the oscillation threshold is reached, and the output power increases dramatically. The output then reaches a maximum and begins to decrease. Due to the imperfections in the PBS, the output coupling ratio reaches a minimum of about 4 % and we see a smoothly varying dip in the output power corresponding to low output coupling and low output power. Here the FOPO is above threshold, but not much power is directed out of the system. As the HWP3 angle increases further, the output power increases once again in a similar fashion and reaches another maximum that is comparable in power to the first peak. A maximum of roughly 50 mW in each sideband could be generated in the symmetric case.

Asymmetric

If we adjust HWP2, FPC, and HWP3 to maximize the output power, and then record the output power as a function of HWP3 angle, the trace becomes asymmetric. In this case (shown in figure 4.2(b)) a small peak in output power occurs followed by a larger peak occurs. The asymmetric mode of operation delivers roughly 28 % more output power than the symmetric mode. The pump field is still plane-polarized in this case except with a slightly lower visibility. Roughly 70 mW in each sideband is generated in the asymmetric case.

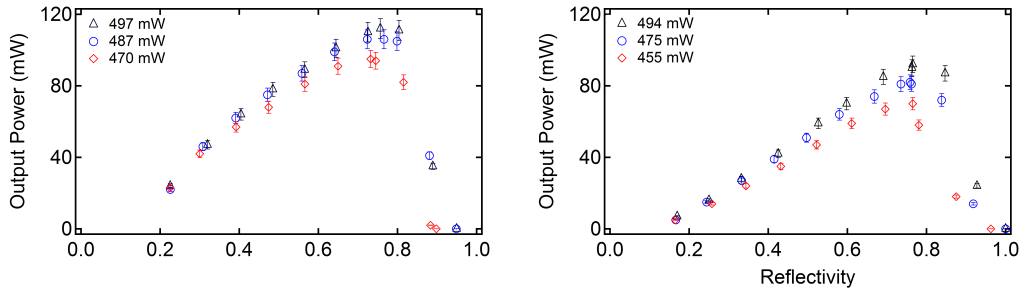

Figure 4.3: Output power versus reflectivity with a PBS as the output coupler for different polarization conditions symmetric (a) and asymmetric (b). We observe that as the gain increases, the reflectivity for optimum output power increases. At high output coupling ratios the FOPO can oscillate even with high losses.

4.1.1 Maximum achievable output coupling

Figure 4.3 (a) illustrates output coupling as a function of the amount of light reflected back into the cavity for symmetric polarization conditions, while figure 4.3(b) is for asymmetric conditions. The range of optimum output coupling corresponds to reflectivities of 0.7-0.8 for both scenarios which is in agreement with the results in Ref. [66]. The important distinction between the two cases is the higher achievable output power in the asymmetric case. The maximum achievable output power for the lowest pumping power in the asymmetric case is comparable to the maximum achievable output power for the highest pumping power in the symmetric case. We observe that the reflectivity for optimum output power increases for increasing input pump powers. However, similar reflectivities yield different output powers depending upon the configurations of the polarization optics. This indicates that reflectivity alone does not determine optimum FOPO operation.

4.1.2 Simulations

We simulate the output coupling polarization dynamics in MATLAB using Stokes vectors. A plane polarization state is first sent through a HWP, and then through a PBS. The orientation of the simulated HWP determines how much energy is reflected out and how much remains in the FOPO cavity. After passing through the PBS, the

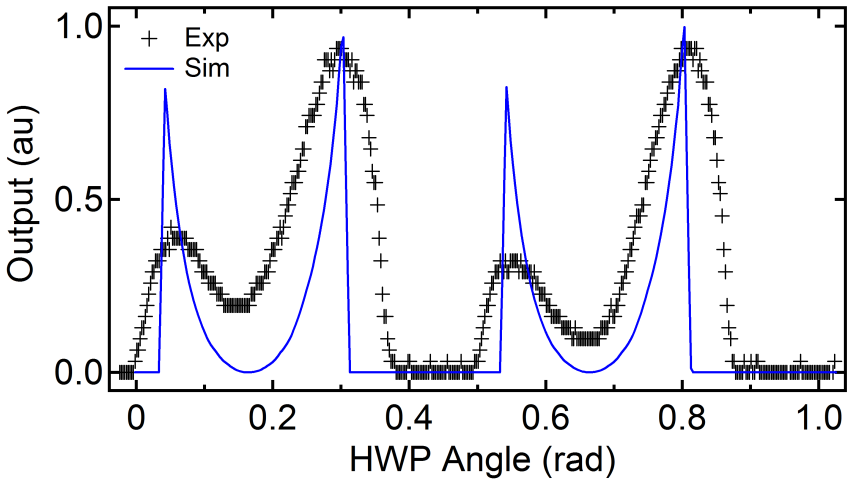

Figure 4.4: Comparison between normalized experimental (black symbols) and simulated (blue lines) output.

field within the FOPO cavity is in a horizontally plane polarized state which is reflected back through the same PBS. The horizontally plane polarized field then passes back through the HWP. The resulting Stokes vector yields the polarization state of the feedback. We can then compare the projection of the feedback Stokes vector with that of the pump, giving a polarization overlap factor. The simulation is repeated for many different configurations of the HWP. We assume that maximum parametric conversion occurs when the feedback polarization state matches the polarization state of the input. Our experimental data is compared to simulated results in figure 4.4. We observe that the simulation captures an asymmetry, but the unevenness is not as large as observed experimentally. We expect that if we were to factor in other degradations comparable to experimental conditions, the output curve would be similar to the observed experimental results.

Our experimental results and simulations indicate that a polarization-based output coupling approach where the polarization varies within our FOPO cavity increases the output power from 50 mW to 70 mW (25 ± 5 %). The use of polarization-based output coupling simplifies the process of controlling the output coupling ratio while maximizing FWM mixing gain as a function of polarization overlap. By increasing FOPO output power while extracting both FWM sidebands, FOPOs become more

attractive for CRS microscopy applications.

We find that the FOPO can be adjusted to oscillate for a wide variety of pump polarization states including plane and elliptical states. Adjusting the half-wave plates and FPC to obtain maximum output power does not necessarily leave the pump in a plane polarization state. In fact, we observe output powers equivalent to our highest observed values for plane and elliptical pump polarizations. For the studies presented here we restrict our observations to the case where the pump is in a plane polarized state at the output of the fiber.

4.2 Intensity noise in FOPOs

Intensity noise has been shown to be significant in fiber-based light sources [69, 70]. Intensity fluctuations well above quantum and instrument levels arise from fluctuations of the pump pulse train [69]. The noise between harmonics of the repetition rate of the pump laser in fiber supercontinuum sources has been observed to rise with pump power from the nonlinear amplification of the pump noise [69–71]. We observe amplification of noise between harmonics of the pump repetition rate in a fiber optical parametric oscillator (FOPO). In figure 4.5 the RF spectrum of the signal sideband of the FOPO is shown for two different pumping powers to demonstrate the increase in the noise between peaks as a function of pumping power.

For multiphoton microscopy, noise in the light source contributes to reduction in the signal-to-noise ratio of the resulting images [10, 55]. This is made evident by examining the CARS signal dependence on the pump and Stokes beams. In the plane wave approximation, the intensity of the CARS signal can be expressed in terms of the pump and Stokes intensities,

$$I_{\mathrm{CARS}} \propto |\chi^{(3)}| I_p^2 I_s L^2 \mathrm{sinc}^2\left(\frac{\Delta k L}{2}\right), \tag{4.1}$$

where $\chi^{(3)}$ is the third order electric susceptibility of the Raman active material, I_p and I_s are the pump and Stokes beam intensities, and L is the material sample thickness [10]. Intensity noise in both the pump and Stokes beams will result in noise

in the CARS signal. If the pump and Stokes beams are generated from the same light source, the CARS signal noise will scale cubically with the pump intensity noise.

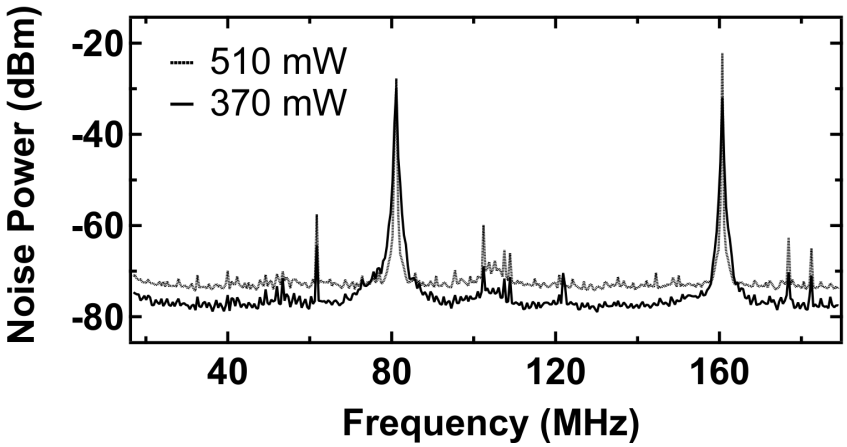

Figure 4.5: Trace of the RF power of a single sideband (signal) for high and low pump powers. The solid line shows the noise power for 370 mW of pump power coupled into the system and the dotted line shows 510 mW. Peaks are located at multiples of the laser repetition rate. Noise power between the peaks increases with pump power. It is important to note the reference level is necessarily low on the electrical spectrum analyzer in order to resolve the background noise so the value at the peaks is not representative of the actual power.

The FOPO measured here is pumped with 8 ps long pulses from a mode-locked Nd:YVO4 laser (Time-Bandwidth Products, Lynx, 80 MHz repetition rate, 1064 nm). The FOPO pump light passes through a half-wave plate (HWP) and isolator before they are injected into a 1.1-m long microstructure optical fiber (MOF) with zero dispersion wavelength located at 1065 nm(NKT Photonics, NL 5.0 1065). Aspheric coupling lenses are placed at the input and output (ThorLabs, C110TME-C and ThorLabs, C220TME-C respectively) of the fiber. Single-pass coupling efficiency for this setup is typically 66 %. The input cleave of the MOF and a translatable end mirror form a Fabry-Perot cavity. There is a fiber polarization controller (FPC) and two half-wave plates before and after the MOF to control the cavity polarization for maximum sideband output power. A prism is placed between the output end of the MOF and the translatable mirror to spectrally filter the light rejected back into the cavity. The FOPO sidebands are tuned by translating and tilting the end mirror of

the cavity, (noted in figure 4.6 as M2), thereby altering the lowest loss wave-length band. Light is coupled out of the cavity via polarization beam splitter (PBS). Typical sideband bandwidths are 3 to 5 nm at 3 dB below the maximum. The pump is filtered away with a notch filter (NF:1064nm) and a variable beam splitter (VBS) serves to attenuate the sideband before the InGaAs photdiode (PD). A diagram of this setup is shown in figure 4.6.

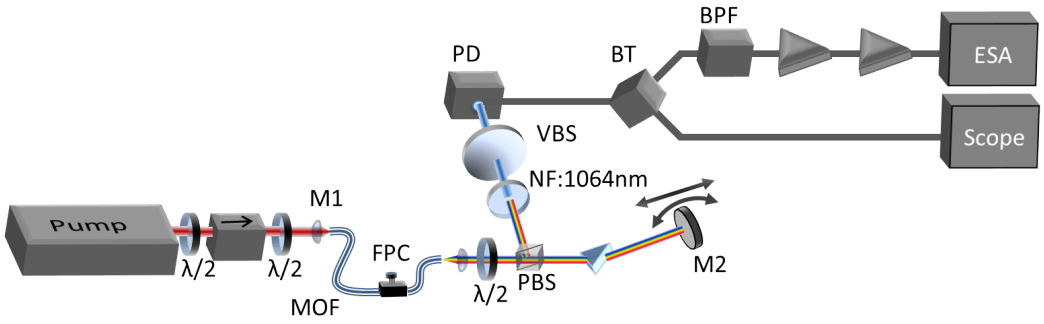

Figure 4.6: (a) Diagram of the FOPO setup.(b) Traces of the FOPO tuning spectra. The pump is located at 1064 nm (right axis). Signal and idler are tuned about 985 nm and 1150 nm respectively (left axis).

The FOPO produces tunable sidebands from 965 nm to 1005 nm and 1130 nm to 1175 nm. A composite of output spectra for the wavelengths used in our measurements is shown in figure 4.6. Due to coupling losses into the optical spectrum analyzer, the optical spectra presented here and throughout this dissertation should not be interpreted as the absolute intensities of the measured light. For a single cavity length setting, excess noise measurements are made for various wavelengths by adjusting only the FOPO cavity end mirror angle. To exploit the full tuning capabilities of this FOPO, this method is applied with three cavity length settings. The alignment settings associated with the highest sideband output powers are in the middle of the angle tuning range for ideal cavity synchronization. The cavity length is adjusted by changing the position of the cavity end mirror.

Either the sideband or filtered supercontinuum signal is detected on an InGaAs detector (EOT 3000).The optical power is attenuated to 5 mW or less before the detector to ensure that the detector does not become saturated. A bias tee splits the

AC and DC components of the detected light. The AC signal from the FOPO and supercontinuum sources are bandpass filtered from 25 MHz to 35 MHz (Mini-circuits BHP-25+, BLP-30+) and 25 MHz to 30 MHz (Minicircuits, BHP-25+, BLP-21.4+) respectively. The filtered signal is amplified in both cases by 44.21 dB in two stages with two RF amplifiers (Minicircuits ZL 1000+). This filtering range is chosen to avoid saturation of the amplifiers. It is important to note that a significant amount of noise is introduced in between the two amplification stages. We do not filter the signal between the amplification stages. This introduces an additional 40 dB overall of noise to the measurement but it does not affect the signal-to-noise ratio.

The amplified signal is sent to the ESA (HP 8592B Spectrum Analyzer). Sample traces are shown in figure 4.7. We measure both the noise level in the unfiltered RF frequency window and the DC level of the signal detected on the photodetector. The noise level in the unfiltered RF frequency window includes contributions from the detection equipment as well as the light source noise. The background noise level is measured by utilizing the same detection scheme with no input light. The background noise level is subtracted from the measured noise level with the input light to isolate contributions from the light source itself.

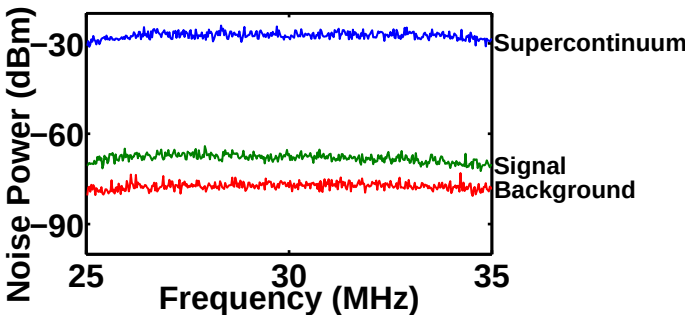

Figure 4.7: Traces of the noise signal for the two light sources in which supercontinuum noise is represented by the blue line and the FOPO level is represented by the green line. The red line represents the instrument noise.

The excess noise is calculated in dBc[Hz] from the noise power in the unfiltered RF window on the ESA and the DC power on the photodetector quantified at the oscilloscope. We calculate excess noise by subtracting the mean background noise from the mean measured noise level, dividing by the DC power and normalizing to

the detection bandwidth of 10 kHz as in the following equation.

$$ExcessNoise = (\frac{N}{P_{DC}B_N}) \tag{4.2}$$

Here N is the average noise power level measured from the trace on the ESA, P_{DC} is the DC power calculated from the voltage on the oscilloscope and B_N is the resolution bandwidth of the measurement. This yields the noise power in a 1 Hz bandwidth relative to the detected DC power.

For the FOPO measurements of excess noise, the input power to the FOPO is maximized to 510 mW. Additionally, sideband output coupling is maximized to approximately 125 mW per sideband with an adjustment of the polarization before the polarizing beam splitter which acts as the output coupler. The input power is also maximized for the supercontinuum configuration. Coupling fluctuations can contribute to low frequency noise in the output fields [72]. In an effort to minimize differences in the coupling contributions to noise the same coupling lens is used for both configurations. The fiber core diameter is 10 μm and the beam spot radius on the fiber tip is 3.2 μm for the FOPO and 4.2 μm for the supercontinuum. The coupling efficiency exceeds 50 % in both configurations. No effort was made to compensate for input pulse chirp from optical elements in the FOPO configuration.

The FOPO excess noise decreases nonlinearly with input power. This is shown in figure 4.8 where FOPO excess noise is plotted as a function pump power. This differs from the linearly increasing trend in supercontinuum excess noise as a function of pump power reported in the literature [70, 71]. At the highest pump power, the excess noise slightly increases. We attribute this increase in noise to the saturation effects in the FOPO. FOPO mirror angle and cavity length tuning were fixed for this measurement and the FOPO has been optimized for highest output power.

For our measurements of excess noise as a function of wavelength, the excess noise of the FOPO output is greater at the extremes of angle tuning compared with that in the middle. This is attributed to relatively poor feedback alignment for these extreme end mirror angles. The FOPO is likely near the threshold of operation at the extreme angles of M2. Since lowest excess noise values usually occur in the

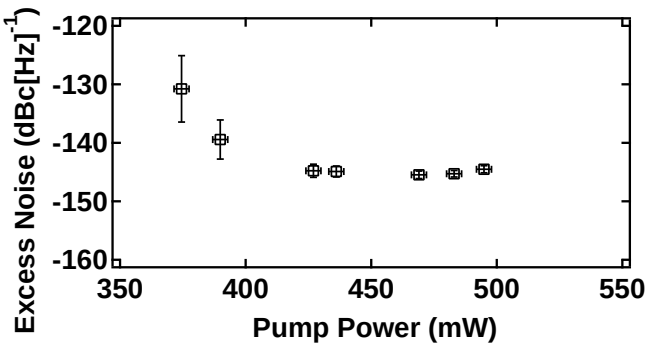

Figure 4.8: Excess noise of FOPO short sideband vs. pump power of the short sideband. The excess noise decreases to a lower limit of -145 dBc$[\mathrm{Hz}]^{-1}$.

middle of the angle tuning range, we suggest that excess noise can be minimized for a broad range of output wavelengths in this FOPO setup by varying the cavity length in conjunction with the end mirror angle. Plots of excess noise level as a function of wavelength restricted to the middle of the angle tuning range for three different cavity length settings are shown in figure 4.8(b) and figure 4.8(d). The corresponding spectra for each excess noise measurement of FOPO sideband are shown in figure 4.8(a) and figure 4.8(c).

Here we have adjusted cavity length and mirror angle to obtain the best excess noise across the full tuning range of the FOPO sidebands. Vertical error bars represent the standard deviation of the mean and the horizontal error bars represent the uncertainty in the center wavelength of each spectral peak. Comparing the FOPO excess noise to that of the excess noise produced by a supercontinuum source, we find that the excess noise produced by the FOPO can be nearly 50 dB lower than the supercontinuum excess noise in a comparable range of spectrum. This is shown in figure 4.11(b) where the excess noise of the supercontinuum is on the order of -95 dBc[Hz] across the measured supercontinuum spectrum compared with -145 dBc[Hz] for a typical FOPO excess noise measurement (see figure 4.11).

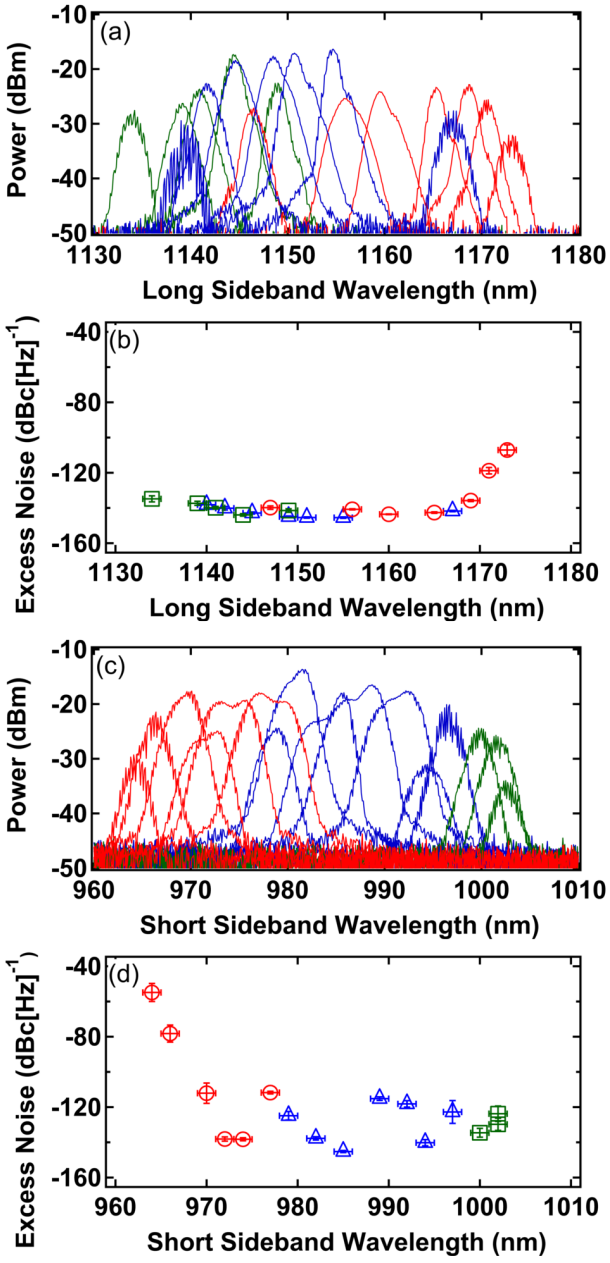

Figure 4.9: (a) Traces of long sideband spectra. (b) Excess noise of FOPO for long sideband spectrum traces. (c) Traces of short sideband spectra. (d) Excess noise of FOPO for short sideband spectrum traces. Red circles, blue triangles and green squares represent measurements for three different cavity lengths of the FOPO.

4.2.1 Comparison to other fiber based light sources

It is not yet known how FOPO noise compares with that of a supercontinuum source. Measurements of the noise performance for a picosecond FOPO and compare them with those of a femtosecond supercontinuum source are shown here. We focus our study on sources of relatively high power (1kW) with narrow-spectrum pulses (1 nm or 1 ps) and sufficient spectral brightness (10mW/nm) for coherent Raman spectroscopy [10].The same type of MOF is employed in both sources. Picosecond pumping was chosen for the FOPO to achieve a practical spectral resolution in the pump and Stokes beams for CARS [55]. Pumping the FOPO with picosecond pulses produces sidebands with spectral bandwidths <10 nm. Femtosecond pumping in the normal dispersion regime was chosen for the supercontinuum generation to produce a spectrum in the same spectral range as the FOPO (shown in figure 4.10). Additionally we report excess noise as a function of input pump power for the FOPO.

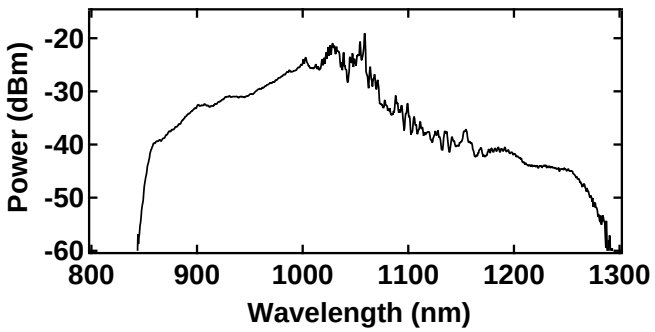

Figure 4.10: Trace of the full supercontinuum spectrum. Pump pulses are 500 fs at 1064 nm.

To generate supercontinuum, 400-fs long pulses from a mode-locked fiber laser (PolarOnyx Inc., Uranus series, 44.7 MHz repetition rate, 1053 nm) are injected into 1.5 m of the same type MOF that is used for the FOPO. This single-pass injection produces a continuous spectrum shown in Fig. 3. The optical spectrum is altered prior to detection (altered peaks are shown in figure 4.11). The three shorter wavelength spectral peaks are produced by introducing dispersion with a prism and spatially selecting spectral bands with a slit. The three longer wavelength peaks are produced

by applying various degrees of tilt to a 10 nm optical bandpass filter centered at 1000 nm (CVI F10-1000). Filtered bandwidths range from 10 nm to 15 nm at 3 dB below their maximum.

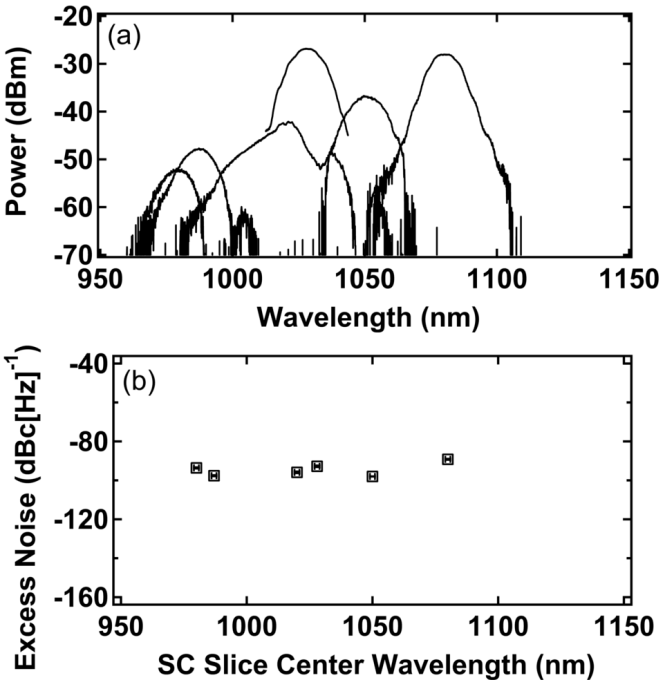

Figure 4.11: (a) Traces of spectral slices of the supercontinuum spectrum. (b) Excess noise of supercontinuum for each slice of spectrum.

Initial stages of broadening for normal dispersion regime pumping of sub-picosecond pulses are governed by self phase modulation. Self phase modulation induced broadening and Raman soliton development near the fiber zero dispersion wavelength causes spectral components to arise in the anomalous dispersion regime. Subsequent broadening of these components is governed by soliton dynamics [7]. The supercontinuum generation process therefore a mixture of self phase modulation, stimulated Raman scattering and soliton dynamics.

Intensity noise in supercontinuum is know to depend on pump pulse chirp. Precise control of input pulse chirp allows for low intensity noise amplification but the amplification rises for modest increases in peak power and chirp. In Ref. [70], the intensity noise is measured over a wide spectrum for various input pump pulse chirps holding

the pulse energy constant (see figure 4.11). The amplification of the input noise is lowest for a small amount of pulse chirp, about 100 fs^2 and grows asymmetrically for increased chirp. Noise growth is rapid for positive and negative chirp and the growth is larger for negatively chirped input pulses. We explored the chirp dependence of excess noise generated in our supercontinuum. The output pulses from our pump laser are compressed by applying chirp at the output. Results are shown in figure 4.12. We find that the excess noise does not exhibit a significant variation in the range of chirps applied here. Furthermore, the noise level does not approach the shot noise level as in Ref. [70]. The main difference in our study is the pulse duration and the range of applied chirps. The 450 fs pulses here are an order of magnitude longer than those in Ref. [70] and our range of applied chirps is significantly smaller. The sign of chirp for this measurement is unknown but the range does not pass through the setting that results in an unchirped pulse. The unchirped pulse setting is assumed to correspond to the micrometer setting for minimum pulse duration, which is near 18 mm. Our range is 22 mm to 24 mm and does not contain the measurement for a minimum pulse duration. The variation in the excess noise measured seems to follow an inverse relationship to the detected power, shown in figure 4.12 on the right axis as photodiode voltage. This implies that there maybe some subtraction or normalization necessary to resolve the chirp effects if they are small.

4.2.2 Discussion

In the best case scenario, the FOPO exhibits excess noise as low as 5 dB above the shot noise level which is about -150 dBc[Hz] for our detection apparatus. This is comparable to the lowest achievable excess noise level of supercontinuum generation in fibers reported in existing literature [69, 70] but with pump pulses that are over two orders of magnitude longer than those used in the referenced supercontinuum implementations. This is advantageous for nonlinear microscopy applications as the optimal excitation pulse durations are hundreds of femtoseconds to a few picoseconds [10]. In accordance with the work in Ref. [71] we would expect to see an increase in the supercontinuum excess noise with the use of longer pump pulses. We measure the

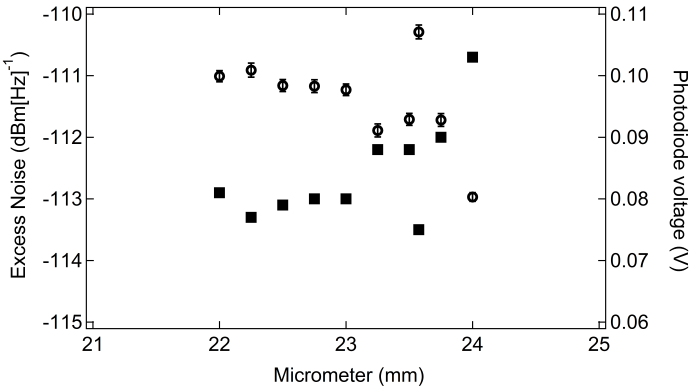

Figure 4.12: Plot of supercontinuum excess noise (left axis) as a function of applied chirp, which is governed by the position of a micrometer in the compressor. The noise does not reduce to near the shot noise level as in [70] and does not change much for the range of applied chirps studied here. The variation in the excess noise measured seems to follow an inverse relationship to the detected power (right axis).

excess noise of our fiber-based supercontinuum source to be 50 dB higher than the lowest supercontinuum excess noise reported in Ref. [70]. The lowest supercontinuum excess noise was achieved by pumping with 50 fs pulses and carefully adjusting the pump pulse chirp. Note that pump pulse durations can be quite different from the pulse durations present in regions of the supercontinuum spectra [73].

The pump pulses used in the FOPO reported here are close to the optimum for CARS [10]. We have also measured the effect of chirp on the noise in our experiments by adjusting the grating compressor of our pump laser but we did not observe any variation in excess noise for the available range of adjustment. It is important to note that the noise level of the pump laser for our FOPO is slightly above the shot noise level and the noise level of the pump laser for supercontinuum was below our detection limit. Our FOPO sidebands are approximately half as wide as the filtered spectra of our supercontinuum. The effect of optical bandwidth in the measurement of noise is studied in Ref. [70] where simulations showed excess noise to increase by 3 dB for a decrease in detected bandwidth from 8 nm to 1 nm. Because of this relationship we do not expect that the difference in the detected optical bandwidths between these sources to be a significant contribution to this comparison. Additionally, the bandwidths of our filter windows vary across the supercontinuum measurements from

10 nm to 15 nm at 3 dB below the maximum however we do not observe the excess noise to vary as a function of bandwidth in our limited range.

We expect that shot noise amplification will scale with the nonlinear phase shift [69], and we can compare the nonlinear phase shift for the FOPO with that of the supercontinuum source for the chosen source parameters. According to the relationship

$$\phi_{NL} = \gamma P L \tag{4.3}$$

where ϕ_{NL} is the nonlinear phaseshift, γ is the fiber nonlinear coefficient, P is the peak power of the pump pulses and L is the fiber length, [48] we estimate that $\phi_{NL} = 10$ for the FOPO and $\phi_{NL} = 500$ for the supercontinuum source. Thus we can expect that the supercontinuum excess noise should be larger than that of the FOPO. There are differences between the two sources presented here such as the pump wavelengths, pump pulse durations and fiber lengths. Also, our supercontinuum pumping regime is not optimized for low intensity noise, however the key idea is that the FOPO is a viable source for CARS as is the supercontinuum source. The noise we study in both sources arises from nonlinear amplification of the input noise, fundamental and otherwise, so the comparison presented here is informative.

Source Type	Pump Pulse Duration	Bandwidth	Minimum Excess Noise
FOPO	8ps	<10 nm	-145 dBc[Hz]$^{-1}$
Supercontinuum	450 fs	10 nm (filtered)	-95 dBc[Hz]$^{-1}$

Table 4.1: Comparison of fiber optical parametric oscillator (FOPO) and supercontinuum (SC) sources.

In conclusion, we find that the FOPO excess noise is large near the threshold for FOPO oscillation and the excess noise decreases as the pump power increases. At FOPO saturation the excess noise reaches a minimum. We find that FOPO excess noise can be as low as -145 dBc[Hz] when the feedback coupling is optimized. The noise level of this FOPO is 50 dB lower than a comparable supercontinuum light

source. Generating the lowest possible noise in supercontinuum requires careful attention to the pump pulse parameters [70]. This may be restrictive to its utilization in coherent Raman scattering microscopy applications. The improvement in excess noise for narrow-band pulses in FOPO's should translate into improvements in the signal-to-noise ratio of CARS images.

Chapter 5

Fiber based single photon sources

A single photon light source is one that supplies one and only one photon in a specified time. One approximate single photon source is a strongly attenuated pulsed laser beam. A pulsed laser provides a beam of photon bunches, or pulses, that fluctuate about a mean number per pulse. If the beam is strongly attenuated one can imagine it begins to look like a source with a single photon per pulse. However, this approach has limitations because the fluctuations in the mean photon numbers per pulse will remain in the attenuated beam. This will not result in a true single photon light source.

Many other platforms exist to generate beams of photons that better approximate the statistics of a single photon beam. In a 2011 review of single photon sources and detectors, a distinction is made between deterministic and probabilistic single photon sources [13]. In deterministic sources, such as quantum dots and single molecule emitters, the generation of single photons is "on-demand". The probabilistic sources, such as spontaneous parametric down conversion or spontaneous four wave mixing, produce photon pairs with some probability that usually scales with the intensity of the optical pumping.

The most widely used probabilistic sources are based on parametric down conversion (SPDC) which produces pairs of entangled photons. These photon pair sources offer an advantage because pairs can be split and their entanglement can be exploited to perform heralding of a single photon stream but the tendency to emit multiple

pairs or zero pairs with some probability limits their usefulness in applications where a photon "on-demand" is needed. Interestingly, entangled photon pairs can be produced "on-demand" in deterministic sources by two photon cascade emission from a biexciton in a quantum dot [74, 75]. However, issues with indistinguishability arise from the jitter in the time that the quantum dot exists in the biexciton state [76].

In this chapter we explore the possibility of producing a fiber-based device for photon pairs with tunable photon number statistics and entanglement properties. Some introductory information on photon number statistics and photon pair entanglement is presented followed by a proposed study in a fiber-based spontaneous four-wave mixing light source.

5.1 Photon number statistics

Probabilistic photon pair sources exhibit a continuum of degrees of nonclassicality depending on what fields are measured (*i.e.*, pairs or single sidebands) and how they are measured. In the following section, the statistical definition and the standards for measurement of a photon beam's nonclassicality are presented.

Photon beams can be classified according to the density fluctuations of photons in the beam. The photons can have a well-defined number distribution over the entire beam, be randomly distributed, or be bunched together in the beam. These situations are referred to as antibunched, coherent or bunched, respectively. Statistically the coherent case follows a Poisson distribution about the mean photon number. An example of a coherent state is the state of a beam of photons emerging from a continuous wave laser. The rate at which photons emerge from the laser fluctuates about a mean value.

An important characteristic of a Poisson distribution is that the variance is equal to the mean of the distribution. The antibunched case has a lower variance than the coherent case and follows a Sub-Poisson distribution. In this case the fluctuations in the rate of photon production from a source are less than that of a laser and can tend to zero. In the bunched situation, the distribution has a greater variance than the mean and follows a Super-Poisson distribution. The fluctuations from a bunched

source can fluctuate to a greater degree than that of a laser and can tend to infinity. A representation of these photon number states is shown in figure 5.1.

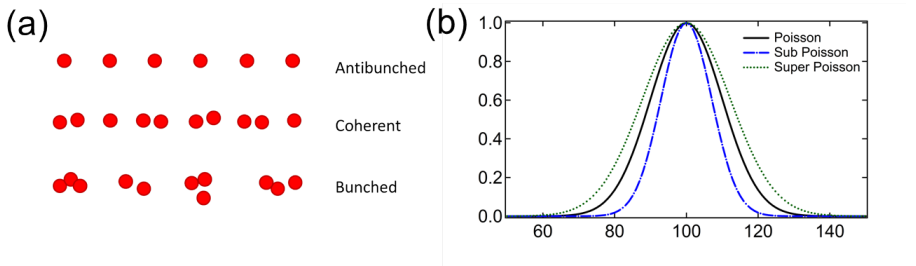

Figure 5.1: (a) Representation of the photon distributions in a beam for the antibunched, coherent and bunched states. (b) Comparison between Poisson, Sub-Poisson and Super-Poisson probability distributions with a mean value equal to 100.

The statistics of a photon stream indicates the degree of quantum mechanical characteristics a light source produces. The Sub-Poisson in a photon stream is an indicator that the light is nonclassical. Nonclassicality is vital for applications of photon number states to quantum information technology [77]. The most strongly nonclassical photon state is referred to as the single photon number state. Characterized by perfect antibunching, it is a state with a mean value of one photon and a variance of zero. Single photon number states are essential for quantum cryptography protocols, such as quantum key distribution [13]. Development in this field has been a strong driver of single photon source development.

5.1.1 Second-order correlation

The development of single photon sources and other nonclassical light sources requires evaluation of the photon number statistics. Photon number statistics are directly determined by studying the correlations within a photon stream. The basic method developed by Hanbury Brown and Twiss is employed to study the correlations in numerous classical and nonclassical light sources. In studying radio astronomy, they developed a novel technique to measure light correlation times which would prove to be essential for the study of quantum states of light. Coherence times were made

evident by carefully examining the output of a beam splitter. In 1956, they reported correlations between the output ports of a beam splitter illuminated by a high-pressure mercury arc. The principles of the HBT experiment would later be employed by Hong, Ou and Mandel to study the statistical properties of photons produced by spontaneous parametric down conversion. The experiment has been adapted to study photon statistics of various states of light [78].

In the classical treatment of the HBT experiment, light impinges on a beam splitter and light from both output ports is sensitively detected. The AC photocurrents from both detectors Δi_1 and Δi_2 are multiplied and the product is time-integrated. The output is proportional to $< \Delta i_1(t)\Delta i_2(t+\tau) >$, which will have large variations for delay times τ that are comparable to the coherence time τ_c [79].

The second-order degree of coherence $g^{(2)}(\tau)$ is given by

$$g^{(2)}(\tau) = \frac{< I_1(t)I_2(t+\tau) >}{< I^2(t) >} \tag{5.1}$$

where I_1 and I_2 are the light intensities after each port of the beam splitter. This is essentially a measurement of the statistics of photons relative to other photons. Because photocurrent is proportional to the intensity, second-order correlations can be observed in the HBT experiment. The second-order correlations can reveal whether light is antibunched, coherent or bunched. While coherent and bunched light can be treated classically, the antibunched case is purely quantum mechanical so the correlations must be written as a function of photon number instead of intensities. The alternative, quantum mechanical, expression for $g^{(2)}(\tau)$ is given by

$$g^{(2)}(\tau) = \frac{< n_1(t)n_2(t+\tau) >}{< n_1(t) >< n_2(t+\tau >} \tag{5.2}$$

where n_1 and n_2 are the photon number counts on the detectors after each port of the beam splitter. The HBT experiment can be modified to detect photon numbers rather than intensities. Detecting coincident photon pairs from both ports as a function of the delay between their arrival times, τ , reveals the number statics of the light.

Coincidence counting, as in the Hanbury Brown Twiss experiments, is depicted in figure 5.2. This is achieved by detecting the two output ports of the beam splitter

on single photon counting modules. A count on one detector is set to trigger a timer. The timer is stopped by a registered count on the other detector. A histogram of counts as a function of the time delay between them can reveal the second-order correlations and thus the photon statistics.

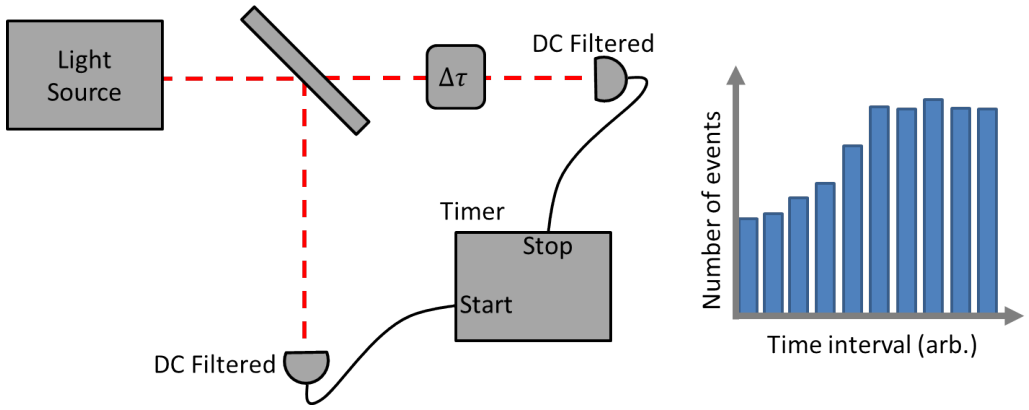

Figure 5.2: Schematic of the Hanbury Brown Twiss experiment with a photon counting detection method. A count on detector 1 triggers the timer to start then a count on detector 2 triggers the timer to stop and the number of counts for a given time interval t is plotted in a histogram. The statistics of these counts indicate the nonclassicality of the light source.

Photons in perfectly antibunched light emerge from their source as single photons with perfect regularity. When this light impinges on a 50-50 beam splitter, each photon will have the same probability of emerging from either port. Before being detected, the photon state is in a superposition of being either transmitted or reflected. When photons are detected at the output ports the delay τ between photons in each output port will be irregular. Additionally, the likelihood of two photons arriving simultaneously at each detector will be small, *i.e.*, the number of coincidence counts at $\tau = 0$ will be small. The consequence in the second order correlation measurement for $\tau = 0$ is

$$g^{(2)}(0) = \frac{< n(n-1) >}{< n >^2} \tag{5.3}$$

which is less than unity. In fact, a second-order correlation function can only take on values less than unity if the light has some degree of nonclassicality [77]. Here,

detecting one photon indicates a low probability of detecting other ones for a certain window of time.

The coincidence counting method can also detect bunched and coherent light. In perfectly coherent light, the average photon number of the light emerging from both ports is constant. This corresponds to $g^{(2)}(\tau) = 1$ because the average photon number remains the same for all delay times τ

$$n_1(t) = n_2(t + \tau) = n \tag{5.4}$$

$$g^{(2)}(t) = \frac{< n^2 >}{< n >^2} = 1 \tag{5.5}$$

so there is no fluctuation in the average photon number state for all inter-photon times τ, *i.e.*, perfect coherence. The case when the light is perfectly random is similar in that the second-order correlation will deviate little from 1 for all times τ. In other words, the detection times for photons in the beam are perfectly independent of each other.

In bunched light, splitting of the photon stream will create two photon streams with a high likelihood of photons with little or no delay from the perspective of the detectors. This will result in a great occurrence of coincidence counts when $\tau = 0$. The second order correlation function will become greater than 1 at $\tau = 0$ and will tend to 1 as $|\tau|$ becomes large. This light is also referred to as chaotic because the fluctuations in processes that depend on a large number of atoms, such as amplified spontaneous emission or the discharge from a mercury lamp, will result in second-order correlation values greater than unity when $\tau = 0$. Here, the detection of a photon indicates a high probability of detecting other ones in a certain window of time.

An important consequence of employing a beam splitter is the consideration of added noise to the detected signals. The input of a consistent stream of photons into one port of a 50-50 beam splitter will result in random noise introduced to each output port of the beam splitter. This is because each photon that arrives at the beam splitter has a 50 % likelihood to be reflected or transmitted. This beam splitter noise does not change the noise on a beam of random, coherent light.

In order to measure the correlation time between two photons produced by SPDC, Hong, Ou and Mandel studied the interference of two photon streams with a Hanbury Brown Twiss photon counting setup [78]. With this technique they were able to measure 50 fs time intervals with an accuracy of 1 fs. This was much faster than the resolution of any photodetector, usually limited to tens of picoseconds, because the broadband nature of the two photon absorption.

The experiment was optically pumped by an argon laser at 351 nm, which passed through 8 cm of potassium dihydrogen phosphate crystal. Some of the incident photons were split into two photons of lower frequency than the pump, such that the resulting photon energies conserved the input photon energy. The two beams of down converted photons were passed through both input ports of a beam splitter. Light from the output ports of the beam splitter was filtered and detected with a coincidence counting scheme. The second order correlation (they refer to this as fourth order correlations) is measured and the correlation time is derived from those data.

The number of coincidences is predicted to tend to zero when the displacement of the beam splitter temporally synchronizes the two paths. Indeed, the data shows a strong dip at this displacement. The width of the dip at the half height is found to be 16 μm, which corresponds to a temporal displacement of 50 fs. The authors mention that one should double this value to 100 fs in order to consider the greater movement in the mirror image. This result is a measurement of the correlation time of the single photon. The authors also mention that visibility will be reduced for measurements of high intensities. The Hong-Ou-Mandel effect is a seminal experiment in quantum interference and has been cited over 1000 times. The characteristic dip in the data suggests that there is a high degree of antibunching, which typifies a strongly nonclassical state of light.

5.2 Dynamic entanglement in optical fibers

Entanglement in photons can be present in various properties such as polarization state, spectrum and spatial extent. Furthermore the degree of entanglement can vary in these properties. An application, such as heralding of a single-photon beam,

can require photons that are entangled but highly uncorrelated. Other applications, such as quantum coherence tomography, require a highly correlated entangled photon source [80]. Generally, photon pairs generated in a nonlinear optical process are produced with correlations in multiple degrees of freedom owing to the conservation of momentum and energy constraints for appreciable gain. Here the photon pairs are considered to be in a quantum mechanical pure state if there are no correlations in all degrees of freedom except for the existence of the pair. Thus, the correlations need to be tailorable in some way to make a source widely applicable.

Type II spontaneous parametric down conversion (SPDC), a $\chi^{(2)}$ process in crystals, is the conventional method for generation of entangled photon pairs [17]. Polarization entanglement in SPDC is commonly studied, as reported in Kwiat *et al.* 1995, because there are numerous high quality polarization control elements available. This method of photon pair production can also be exceptionally bright, but it has many limitations. For instance, the output is multimode which can be undesirable in experiments where high purity of output states is required. Post-generation filtering is used to overcome this challenge. Filtering of both the spatial and the spectral modes is achieved by utilizing a waveguide, but this results in a great loss in the brightness [81].

A clever way to circumvent post-generation spatial and spectral filtering is to utilize the narrowband nature of spontaneous four wave mixing in optical fibers, suggested in Grice *et al.* [82]. Although SFWM is a $\chi^{(3)}$ process which has a smaller interaction strength than the $\chi^{(2)}$ processes, the long interaction length in fiber can compensate for this to achieve comparable brightness [41]. This method offers a number of advantages in the collection efficiency, scalability and compactness owing to the fiber architecture. Additionally, there is an important implication in the entanglement properties that arise from a particular combination of pump wavelength and fiber dispersion. The ability to dexterously modify this combination allows for dynamic tuning of entanglement properties [83]. This amounts to tuning the pump wavelength in a range between two zero dispersion wavelengths, which allows for dynamic tuning of entanglement properties in pairs of photons.

Challenges

A key challenge in photon pair generation in fibers is the strong spontaneous Raman scattering in silica fibers that results in productions of red shifted photons over a broad spectrum of up to 40 THz that peaks at 13 THz from the input frequency [48]. The deleterious effects from Raman scattering can be overcome by utilizing a setup that produces sidebands more than 40 THz away from the pump, thus being outside of the Raman gain region [84].

In a review of this topic, Raymer and Srinavasan mention that a limiting aspect of state preparation in $\chi^{(3)}$ devices is the ability to make fiber cores uniform for long fiber length [16]. In Clark *et al.*, [85] a birefringent microstructure optical fiber is used to maximize the intrinsic narrowband sideband generation through SFWM in photonic crystal fiber. They find that spectral bandwidth decreases with an increase in fiber length. The narrowband emission is desirable for entanglement tailoring but they mention that inhomogeneity in the fiber microstructure limited their test fiber to 1 m.

Manipulating the JSI

Photon pairs are usually produced in a mixed state of entanglement. An advantage of generation in fibers over the SPDC method is that the photon pairs can be made to generate into a single mode, while complex dispersion tailoring can further eliminate undesired correlations in order to increase the purity of the photon pair state [83, 86]. In fact, photon pairs from SFWM in fibers can range from a mixed, highly entangled state to a pure, factorable or minimal entanglement state. This is not available or at least very difficult in the SPDC sources because factorable states require spatial and spectral entanglement to be minimized. SFWM emission into the single mode of a fiber easily offers the minimal spatial entanglement, whereas SPDC sources are multimode and require filtering to achieve the same state. SFWM photon pairs are factorable when the pair-photon state is expressible as a product of the signal and the idler state *i.e.* $|\Psi>= |0>_S |0>_I + \kappa |1>_S |1>_I$. This is made more obvious when examining a plot of the joint spectral amplitude (JSA), defined as the square root of

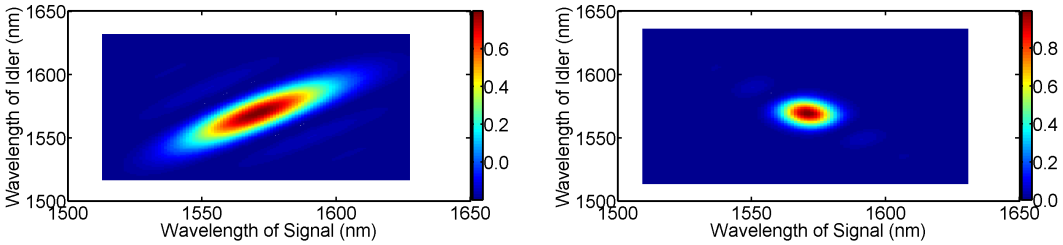

Figure 5.3: The shape of the joint spectral intensity (JSI) indicates the level of entanglement in a photon pair. (a) JSI with distribution along a linear positive slope shown here indicates strong spectral correlation in the signal and idler photon pairs. (b) JSI with centered distribution shown here indicates minimal spectral correlation and thus a potentially pure or factorable photon pair.(JSIs generated in SPDCalc [87].

the joint spectral intensity (JSI) of the SFWM setup [83]. The mathematical details are presented in Appendix section 1, graphically the JSA represents the gain spectrum of SFWM for a particular setup where the signal wavelength is plotted against the idler wavelength over a given range. Various manipulations to the setup can be made to change the shape and slope of the JSA or JSI. Two examples of possible JSIs are shown in figure 5.3. The alignment of the long axis in the JSI is essentially a visualization of the entanglement properties. This shape and the alignment can change with the phase matching and group velocity matching in a SFWM setup.

The JSA is the product of the pump envelope function $\alpha(\omega_p)$ and the phase matching function $\Delta k(\omega_p, \omega_s, \omega_i)$. The pump envelope function is usually assumed to be Gaussian with some width, σ_p. In the degenerate pumping case, the pump envelope function plotted in the signal vs. idler spectrum axes is a set of contours that are constant along the lines defining $\omega_s + \omega_i = const.$ and having a Gaussian shape in the direction transverse to these contour lines. The phase matching function has the transverse shape of a sinc function in the JSA (sinc^2 in the JSI) that has contours of constant value for $\Delta k = const.$ maximized at $\Delta k = 0$. The relative angle between these constant contours in these two functions influences the produced shape in the JSA. When the long axis of the JSA is parallel to an axis of the plot, the correlations have been minimized. Symmetric JSAs with no long or short axes also are minimally correlated.

In Garay-Palmett *et al.*, phase and group velocity matching requirements are

achieved through placement of the pump, signal and idler fields about the zero-dispersion wavelength [83]. Tuning of the pump wavelength, shifts the angle of the contours in the phase matching function and thus tunes the JSA shape. This can also be achieved through the tailoring of birefringence in the optical fiber [88–91]. Here, two pumps propagate along the slow axis of the fiber and the signal and idler travel along the fast axis. Several routes exist for experimentally phase and group velocity matching in optical fibers. The advantage in the birefringence method is the added conversion efficiency from pump to pair-states.

5.3 A proposed study

Several interesting measurements can be made on a source of photon pairs. They can be split up and the detection of one photon in the pair heralds or indicates the existence of the other in the pair. Correlation times can be measured in various combinations of fields. Power dependence of the statistics can be explored.

In order address some practical challenges, the ideal fiber based photon pair source would have a spontaneous four wave mixing gain spectrum that peaks outside of the Raman gain region in the fiber. If this fiber were made of silica, it would need to have a gain peak greater than 40 THz away from the pump wavelength. This is necessary to avoid additional spontaneously scattered Raman photons in the red shifted region of spectrum to interfere with the heralding of photons in the blue shifted spectrum. In order to maximize the dexterity in tuning of the entanglement properties, this fiber would need to be single mode for all the wavelengths involved and the group velocity dispersion should match for all wavelengths as well. This ensures spatial correlations are minimal. Such a fiber would need to generate four wave mixing sidebands and be designed with two zero dispersion wavelengths (ZDWs). All of these fiber design requirements can be achieved in microstructure optical fibers.

In order to traverse through the varied entanglement scenarios as proposed in the pump tuning manipulation of the JSI, the pump laser should be tunable in the range between the two zero dispersion wavelengths [83]. The SFWM gain can be experimentally verified by injecting a high power pump and observing the output

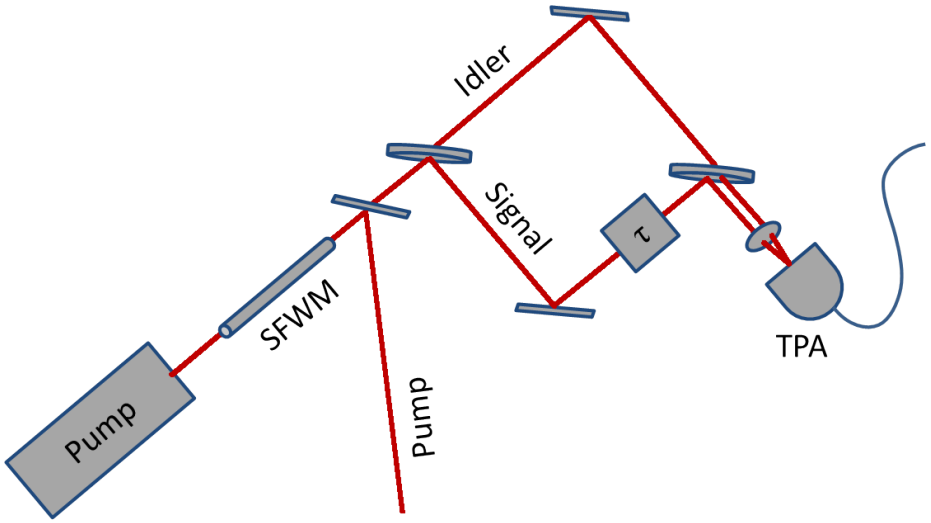

Figure 5.4: Schematic of two-photon absorption scheme for measuring the second order correlation function. Correlated pairs of photons are generated through SFWM in an optical fiber. The pump and is filtered away from the correlated photons. The signal and idler are separated using a dichroic beamsplitter then directed onto a two-photon absorbing photodiode. When there is no delay between optical paths taken by signal and idler, $\tau = 0$, photon statistics are observable in the photocurrent generated in the TPA detector.

spectrum. Intensity should grow simultaneously in the sidebands as the pump power is increased. It may be the case that the designed fiber dispersion does not match the fabricated fiber dispersion, so experimental verification of the ZDWs and phase matching curves is important for an ideal photon pair source.

A schematic of the proposed experiment is shown in figure 5.4. Once the sidebands are generated, one can measure the correlation times of the signal and idler photons. These photons are born in pairs so they should be strongly bunched. Second order correlation measurements would reveal the degree of bunching and the correlation time. Because they are created simultaneously, the correlation time is expected to be very short. Coincidence detection can be thought of as limited to the time sensitivity of the detector, which is usually in the tens of picoseconds. The second order coherence measurement at $\tau = 0$ is only significantly measurable when the correlation time is on the order of the detection time response. Photon pair pulses can be much shorter in time and the correlation times are expected to be much shorter.

In one study aimed at measuring the photon statistics of black-body radiation, a process with very short correlation times on the order of a few femtoseconds, the semiconductor properties of a GaAs photomultiplier tube, were exploited to perform two-photon absorption [92]. Two-photon absorption allows for any two photons of energy that sums to the semiconductor gap between the conduction band and the valence band to generate a detection response. This makes the measurements broad-band and thus very sensitive temporally. Boiter *et al.* applied the same technique to study the degree of second-order coherence for twin beams of down-converted light and they find that they are able to resolve the coherent and incoherent contributions to g^2 [93]. It is also possible to use $\chi^{(2)}$ nonlinearities in crystal to optically detect ultrafast coherence measurements [94, 95]. It is expected that g^2 can exhibit anti-bunching even for relatively large numbers of photons [96]. To the best of our knowledge, correlation times for SFWM signal and idler photons have not been previously measured with this two photon absorption detection technique.

An important verification to perform on this detection method would be to measure the second order correlation of the pump with itself. It should display coherent state characteristics, described in the section above, meaning that the second order correlation should be equal to unity over the entire range. The correlation time for a single sideband with itself is another interesting experiment. It is expected that a single sideband should exhibit nonclassicality in the second order correlation. It is also expected that this will change a function of the pumping power, resulting in a transition between the classical and nonclassical states of light [41]. A schematic of the proposed additional second order correlation measurements is shown in figure 5.5.

5.4 Preliminary data

A commercially available microstructure optical fiber has been investigated preliminarily for potential use as a SFWM source of photon pairs. About 10 cm of SC 1040 fiber, obtained from Thorlabs, is pumped by about 800 mW of 1053 nm laser light pulsed at a repetition rate of 44.7 MHz. The pulses are assumed to be fully compressed to about 450 fs. SFWM is exhibited in figure 5.6 with sidebands peaking

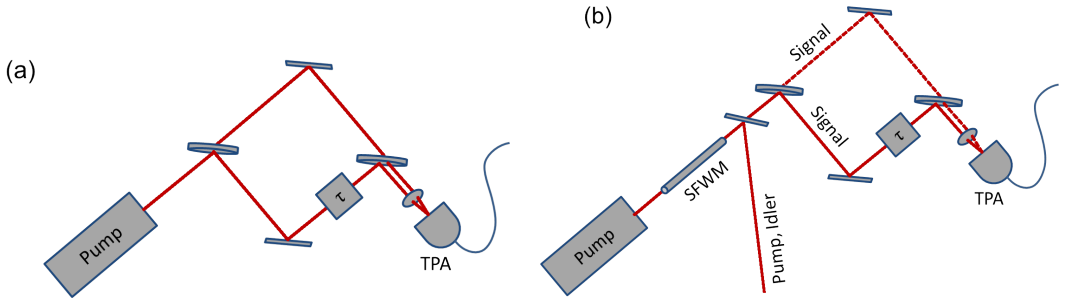

Figure 5.5: Schematic of second-order correlation measurements for, (a), pump field only and, (b), signal sideband. The pump-pump correlation is expected to show the properties of a coherent state and result in unity of all values of τ. The signal-signal correlation is expected to display some degree of nonclassicality which is dependent on the input power.

at 930 nm and 1200 nm.

A simple semicondutor photodiode is used as the two photon absorption detector. It is a Hamamatsu G115 made of GaAsP with a sensitivity spectrum that ranges from 300 nm to 700 nm peaked at about 600 nm with a maximum response of 0.3 A/W. The detection response is characterized to be in the two photon absorption regime, with a power response curve of only the pump. A pump wavelength at 1053 nm results in a two photon absorption sensitivity at 527 nm, which is within the sensitivity curve of this detector. The characteristic quadratic response, shown in figure 5.7, indicates the detector is indeed working in the two photon absorption detection regime.

The threshold of optical power needed to detect light in this setup is found to be about a few mW. At the time of this characterization, the maximum achievable sideband power at the detection location was 1.79 mW. The dynamic range of detection in this manner is therefore not suitable for the sideband correlation experiments. This can be improved by managing coupling and reflection losses in the sidebands or by using a more sensitive photodiode in the two photon detection scheme.

A similar experiment has been performed in house with slightly different equipment and conditions. In this experiment, the two photon absorption signal is observed as a function of delay between sidebands produced by self phase modulation in SC 1040 fiber pumped by a pulsed laser source at 1053 nm. Note that these are the same

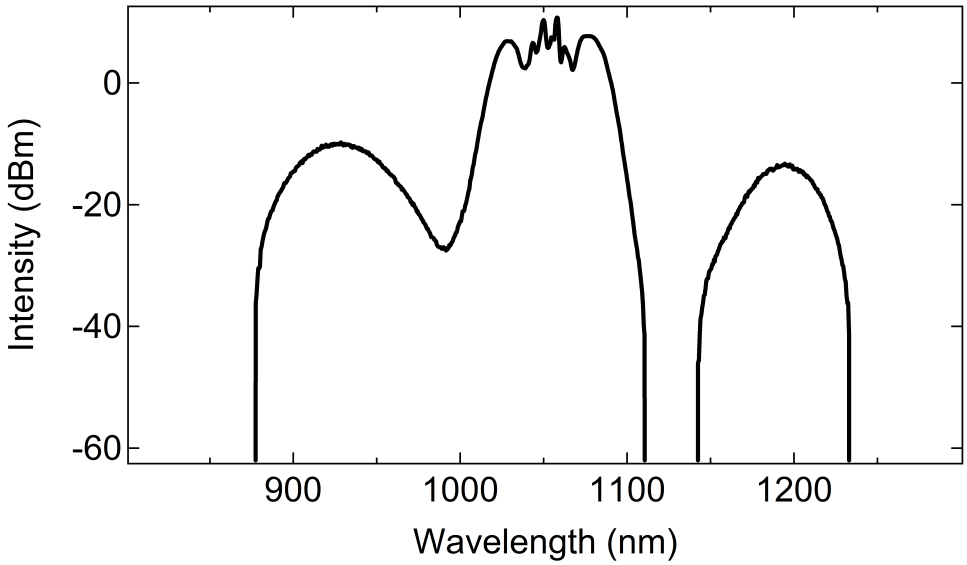

Figure 5.6: Spontaneous four wave mixing spectrum of 10 cm of SC 1040 fiber. The coupling efficiency for this measurement was 35% with an input power of 860 mW.

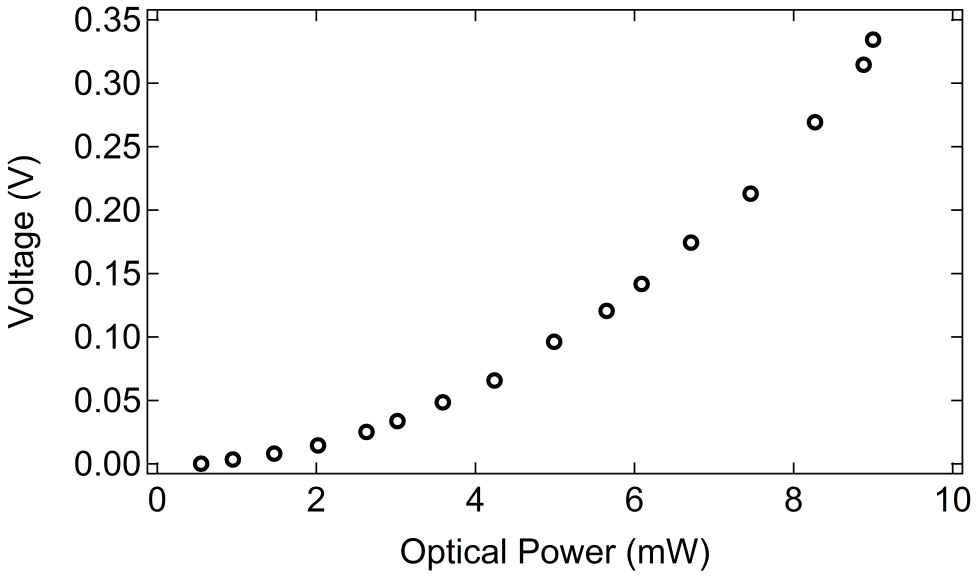

Figure 5.7: This plot shows the characteristic quadratic response of two photon absorption detection of a 1053 nm pulsed fiber laser (PolarOnyx Inc., Uranus series, 44.7 MHz repetition rate, 1053 nm) by an GaAsP photodetector (Hammamatsu G115).

fiber type and laser source mentioned in the previous experiment but the nonlinear effect is different. Also the detector used here is a silicon photodiode. The results from this experiment are shown in figure 5.8.

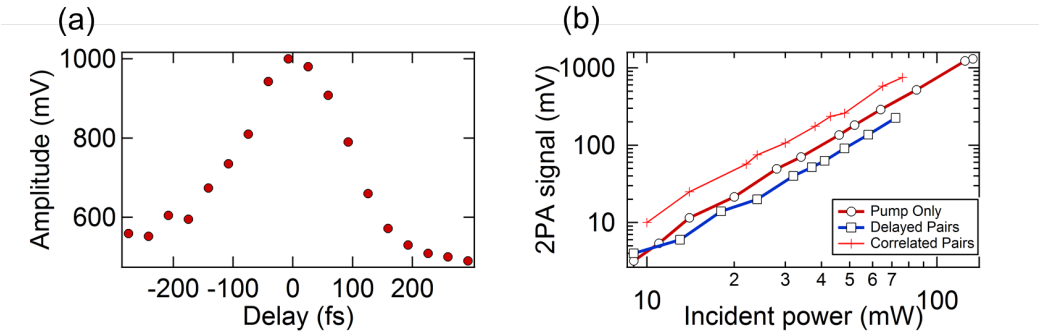

Figure 5.8: (a) Two photon absorption signal as a function of delay between sidebands produced by self phase modulation. Coherence time is on the order of 100 fs (b) Quadratic response of detection for the pump only, the uncorrelated pairs and the highly correlated pairs ensuring that all three are in the two photon absorption detection regime on a silicon photodetector.

At zero delay we observe photon bunching and a correlation time on the order of 100 fs. When the delay is increased beyond the correlation time of the source then the photons appear uncorrelated as in a coherent source. By comparing the signal at the peak with that in the wings in figure 5.8 we see that $g^{(2)}(0) = 2$. Figure 5.8(b) is a plot of two photon absorption signal as a function of incident power. One expects a quadratic response as a function of power because two photon absorption is dominating over linear absorption. From these measurements we conclude that $g^{(2)}(\tau)$ measurements are possible using two photon absorption and they are likely to lead to insight into the nature of correlated twin beams of photons.

Chapter 6

Conclusions and future prospects

The main achievements of this dissertation are summarized below:

- Improved power output of a fiber OPO with an original polarization-based output coupling method that exploits the polarization dynamics within the FOPO cavity. We demonstrated an improved design for performance of a fiber optical parametric oscillator. The improved output power was achieved by optimizing the system for both output coupling ratio and polarization overlap withing the fiber.

- Demonstration of the improved intensity noise performance of FOPOs when compared to fiber-based continuum sources. We compared intensity noise arising from amplification of technical noise in two fiber-based sources designed for CRS microscopy. The fiber optical parametric oscillator was shown to have more desirable properties than a supercontinuum source.

- Dispersion measurement of soft glass microstructure optical fibers. We applied the Fourier transform spectral interferometry method for dispersion measurement to highly nonlinear soft glass microstructure optical fibers. We used a Raman shifted soliton to pump further into the IR spectrum. We measured

dispersions near to that of the bulk material but without good agreement with theoretical dispersion curves.

- Continuum generation marked by strong soliton dynamics in soft glass microstructure optical fiber. We generated dispersive waves in SF57 microstructure fiber by pumping with a high power Raman shifted soliton.

- Proposal of nonclassicality measurement on entangled photon pairs generated by spontaneous four wave mixing in microstructure optical fiber using two-photon absorption detection. We show how photon pairs of various degrees of entanglement can be generated in optical fiber and they can be efficiently detected using two-photon absorption in a regular photodiode.

Some projects attempted during this dissertation that will be passed along to later generations of students:

- Two photon absorption detection of nonclassical light from a fiber parametric device
- Utilizing soft glass microstructure fibers in a parametric device

- Development of a directly modulated and tunable pump for a fiber optical parametric oscillator

- Intensity noise measurements of a Ti:Sapph pumped fiber optical parametric oscillator

Appendix A

Appendix

A.1 Joint Spectral Intensity

The following mathematical description of the joint spectral amplitude is summarized from Garay-Palmett *et al.* [83]. Generally the state of a photon pair generated by spontaneous four wave mixing can be written

$$|\Psi\rangle = |0\rangle_s|0\rangle_i + \kappa \int\int d\omega_s d\omega_i F(\omega_s, \omega_i)|\omega_s\rangle_s|\omega_i\rangle_s \tag{A.1}$$

where κ is a constant representing the generation efficiency, ω_s and ω_i are the signal and idler frequencies respectively, and $F(\omega_s, \omega_i)$ is the joint spectral amplitude (JSA). The JSA is written

$$F(\omega_s, \omega_i) = \int d\omega' \alpha_1(\omega')\alpha_2(\omega_s+\omega_i-\omega')\times \mathrm{sinc}\left[\frac{L}{2}\Delta k(\omega', \omega_s, \omega_i)\right] \exp\left[i\frac{L}{2}\Delta k(\omega', \omega_s, \omega_i)\right] \tag{A.2}$$

where $\alpha_{1,2}$ are the pump spectral amplitudes and $\Delta k(\omega', \omega_s, \omega_i)$ is the phase mismatch. Assuming that all fields are co-polarized the phase mismatch is expressed as

$$\Delta k(\omega', \omega_s, \omega_i) = k(\omega_1) + k(\omega_s + \omega_i - \omega_1) - k(\omega_s) - (\gamma_1 P_1 + \gamma_2 P_2) \tag{A.3}$$

which includes wave vectors, k, of all four fields as well as self and cross phase modulation terms, γP. A factorable state is one where the joint spectral amplitude can be written as the product of two functions *i.e.*$F(\omega_s, \omega_i) = S(\omega_s)I(\omega_i)$ where the functions $S(\omega_s)$ and $I(\omega_i)$ depend only on the signal and idler frequencies respectively.

It is possible to write the joint spectral amplitude in closed analytical form with the appropriate assumptions. Assuming the pump envelope function, $\alpha(\omega)$ to be a Gaussian function of width, σ_p and making use of a linear expansion in the phase mismatch, Δk the following expression of the joint spectral amplitude can be written

$$F_{lin}(\nu_s, \nu_i) = \alpha(\nu_s, \nu_i)\phi(\nu_s, \nu_i) \quad = \exp\left[-\frac{(\nu_s + \nu_i)^2}{\sigma_1^2 + \sigma_2^2} \right] \mathrm{sinc}\left[\frac{L\Delta k_{lin}}{2} \right] \exp\left[i\frac{L\Delta k_{lin}}{2} \right]$$

where the detunings, ν, are defined $\nu_s = \omega_s - \omega_s^0$ and $\nu_i = \omega_i - \omega_i^0$. More details of this derivation are given in reference [83].

The final expression of the joint spectral amplitude shows a product of exponentials and a sinc function. In the signal vs. idler spectral axes, the pump envelope function extends along a line defined as $\omega_s + \omega_i = 2\omega_p$ and the phase matching function extends along a line defined as $\Delta k = 0$. The relative alignment of these lines determines the final shape and alignment of the JSI and thus the entanglement properties. The sinc function in the phase matching expression contributes the lobes to the overall JSI.

Bibliography

[1] About the year of light. *http://www.light2015.org/Home/About.html*, 2015.

[2] Gianluca Geloni, E Saldin, L Samoylova, E Schneidmiller, H Sinn, Th Tschentscher, and M Yurkov. Coherence properties of the european xfel. *New Journal of Physics*, 12(3):035021, 2010.

[3] T Kessler, C Hagemann, C Grebing, T Legero, U Sterr, F Riehle, MJ Martin, L Chen, and J Ye. A sub-40-mhz-linewidth laser based on a silicon single-crystal optical cavity. *Nature Photonics*, 6(10):687–692, 2012.

[4] M Hentschel, R Kienberger, Ch Spielmann, Georg A Reider, N Milosevic, Thomas Brabec, Paul Corkum, Ulrich Heinzmann, Markus Drescher, and Ferenc Krausz. Attosecond metrology. *Nature*, 414(6863):509–513, 2001.

[5] Ximao Feng, Steve Gilbertson, Hiroki Mashiko, He Wang, Sabih D Khan, Michael Chini, Yi Wu, Kun Zhao, and Zenghu Chang. Generation of isolated attosecond pulses with 20 to 28 femtosecond lasers. *Physical review letters*, 103(18):183901, 2009.

[6] CD Macchietto, BR Benware, and JJ Rocca. Generation of millijoule-level soft-x-ray laser pulses at a 4-hz repetition rate in a highly saturated tabletop capillary discharge amplifier. *Optics letters*, 24(16):1115–1117, 1999.

[7] John M Dudley, Goëry Genty, and Stéphane Coen. Supercontinuum generation in photonic crystal fiber. *Reviews of modern physics*, 78(4):1135, 2006.

[8] ME Klein, CK Laue, D-H Lee, K-J Boller, and R Wallenstein. Diode-pumped singly resonant continuous-wave optical parametric oscillator with wide continuous tuning of the near-infrared idler wave. *Optics letters*, 25(7):490–492, 2000.

[9] MMJW Van Herpen, SE Bisson, AKY Ngai, and FJM Harren. Combined wide pump tuning and high power of a continuous-wave, singly resonant optical parametric oscillator. *Applied Physics B*, 78(3-4):281–286, 2004.

[10] Ji-Xin Cheng and Xiaoliang Sunney Xie. *Coherent Raman scattering microscopy*. CRC press, 2012.

[11] Roy J Glauber. Nobel lecture: One hundred years of light quanta. *Reviews of modern physics*, 78(4):1267, 2006.

[12] Rodney Loudon. *The quantum theory of light*. Oxford university press, third edition, 2000.

[13] MD Eisaman, J Fan, A Migdall, and SV Polyakov. Invited review article: Single-photon sources and detectors. *Review of Scientific Instruments*, 82(7):071101, 2011.

[14] Albert Einstein. Uber einen die erzeugung und verwandlung des lichtes betreffenden heurischen gesichtpunkt. *Ann. Phys.*, 17:132–148, 1905.

[15] Robert Andrews Millikan. A direct photoelectric determination of planck's" h". *Physical Review*, 7(3):355, 1916.

[16] Michael G Raymer and Kartik Srinivasan. Manipulating the color and shape of single photons. *Physics Today*, 65(11):32–37, 2012.

[17] Paul G Kwiat, Klaus Mattle, Harald Weinfurter, Anton Zeilinger, Alexander V Sergienko, and Yanhua Shih. New high-intensity source of polarization-entangled photon pairs. *Physical Review Letters*, 75(24):4337, 1995.

[18] Jingyun Fan and Alan Migdall. A broadband high spectral brightness fiber-based two-photon source. *Optics express*, 15(6):2915–2920, 2007.

[19] Andrew J Shields. Semiconductor quantum light sources. *Nature photonics*, 1(4):215–223, 2007.

[20] Charles H Bennett. Quantum cryptography using any two nonorthogonal states. *Physical Review Letters*, 68(21):3121, 1992.

[21] Klaus Suhling, Paul MW French, and David Phillips. Time-resolved fluorescence microscopy. *Photochemical & Photobiological Sciences*, 4(1):13–22, 2005.

[22] I Rech, A Restelli, S Cova, M Ghioni, M Chiari, and M Cretich. Microelectronic photosensors for genetic diagnostic microsystems. *Sensors and Actuators B: Chemical*, 100(1):158–162, 2004.

[23] Jens-Peter Knemeyer, Nicole Marme, and Markus Sauer. Probes for detection of specific dna sequences at the single-molecule level. *Analytical chemistry*, 72(16):3717–3724, 2000.

[24] Takashi Isoshima, Yasushi Isojima, Katsuhiko Hakomori, Kazuro Kikuchi, Katsuya Nagai, and Hachiro Nakagawa. Ultrahigh sensitivity single-photon detector using a si avalanche photodiode for the measurement of ultraweak biochemiluminescence. *Review of scientific instruments*, 66(4):2922–2926, 1995.

[25] Maurizio Viterbini, Alberto Adriani, and Guido Di Donfrancesco. Single photon detection and timing system for a lidar experiment. *Review of scientific instruments*, 58(10):1833–1839, 1987.

[26] M Ware and A Migdall. Single-photon detector characterization using correlated photons: the march from feasibility to metrology. *Journal of Modern Optics*, 51(9-10):1549–1557, 2004.

[27] PA Franken, AE Hill, CW el Peters, and G Weinreich. Generation of optical harmonics. *Physical Review Letters*, 7(4):118, 1961.

[28] M Bass, PA Franken, JF Ward, and G Weinreich. Optical rectification. *Physical Review Letters*, 9(11):446, 1962.

[29] SA Akhmanov and RV Khokhlov. Concerning one possibility of amplification of light waves. *Sov. Phys. JETP*, 16:252–257, 1963.

[30] RW Terhune, PD Maker, and CM Savage. Optical harmonic generation in calcite. *Physical Review Letters*, 8(10):404, 1962.

[31] EJ Woodbury and WK Ng. Ruby laser operation in near ir, 1962.

[32] N. Bloembergen. Nonlinear optics: past, present, and future. *Selected Topics in Quantum Electronics, IEEE Journal of*, 6(6):876–880, Nov 2000.

[33] Jeff Squier and Michiel Müller. High resolution nonlinear microscopy: A review of sources and methods for achieving optimal imaging. *Review of Scientific Instruments*, 72(7):2855–2867, 2001.

[34] D Brüggemann, J Hertzberg, B Wies, Y Waschke, R Noll, K-F Knoche, and G Herziger. Test of an optical parametric oscillator (opo) as a compact and fast tunable stokes source in coherent anti-stokes raman spectroscopy (cars). *Applied Physics B*, 55(4):378–380, 1992.

[35] ES Polzik, J Carri, and HJ Kimble. Spectroscopy with squeezed light. *Physical review letters*, 68(20):3020, 1992.

[36] Govind P. Agrawal. Nonlinear fiber optics: its history and recent progress. *J. Opt. Soc. Am. B*, 28(12):A1–A10, Dec 2011.

[37] Rogers H. Stolen. Phase-matched-stimulated four-photon mixing in silica-fiber waveguides. *Quantum Electronics, IEEE Journal of*, 11(3):100–103, Mar 1975.

[38] L.G. Cohen, Chinlon Lin, and W.G. French. Tailoring zero chromatic dispersion into the 1.51.6 m low-loss spectral region of single-mode fibres. *Electronics Letters*, 15(12):334–335, June 1979.

[39] J. Teipel, K. Franke, D. Turke, F. Warken, D. Meiser, M. Leuschner, and H. Giessen. Characteristics of supercontinuum generationin tapered fibers using femtosecond laser pulses. *Applied Physics B*, 77(2-3):245–251, 2003.

[40] Tanya M. Monro and Heike Ebendorff-Heidepriem. Progress in microstructured optical fibers. *Annual Review of Materials Research*, 36(1):467–495, 2006.

[41] Elizabeth A Goldschmidt, Matthew D Eisaman, Jingyun Fan, Sergey V Polyakov, and Alan Migdall. Spectrally bright and broad fiber-based heralded single-photon source. *Physical Review A*, 78(1):013844, 2008.

[42] William Wadsworth, Jonathan Knight, and Tim Birks. State-of-the-art photonic crystal fiber. *Optics and Photonics News*, 23(3):24–31, 2012.

[43] TA Birks, PJ Roberts, P St J Russell, DM Atkin, and TJ Shepherd. Full 2-d photonic bandgaps in silica/air structures. *Electronics letters*, 31(22):1941–1943, 1995.

[44] Govind P Agrawal. *Fiber-optic communication systems*, volume 1. Wiley, 1997.

[45] Wen Qi Zhang, Shahraam Afshar V, and Tanya M Monro. A genetic algorithm based approach to fiber design for high coherence and large bandwidth supercontinuum generation. *Optics express*, 17(21):19311–19327, 2009.

[46] Wen Qi Zhang, Heike Ebendorff-Heidepriem, Tanya M Monro, and Shahraam Afshar V. Fabrication and supercontinuum generation in dispersion flattened bismuth microstructured optical fiber. *Optics express*, 19(22):21135–21144, 2011.

[47] Unknown Author. Extending opportunities. *Nat Photon*, 6(7):407, 2012.

[48] Govind P Agrawal. *Nonlinear fiber optics*. Academic press, 2007.

[49] Periklis Petropoulos, Heike Ebendorff-Heidepriem, Vittoria Finazzi, Roger Moore, K Frampton, D Richardson, and T Monro. Highly nonlinear and anomalously dispersive lead silicate glass holey fibers. *Optics Express*, 11(26):3568–3573, 2003.

[50] Robert W Boyd. *Nonlinear Optics*. Academic Press, 2008.

[51] Kunimasa Saitoh, Nikolaos Florous, and Masanori Koshiba. Ultra-flattened chromatic dispersion controllability using a defected-core photonic crystal fiber with low confinement losses. *Optics Express*, 13(21):8365–8371, 2005.

[52] Leonard G Cohen. Comparison of single-mode fiber dispersion measurement techniques. *Lightwave Technology, Journal of*, 3(5):958–966, 1985.

[53] Leily Kiani, Tilanka Munasinghe, Wen Qi Zhang, Shahraam Afshar, and Jay Sharping. Linear and nonlinear properties in soft glass optical fibers for device applications. In *APS March Meeting Abstracts*, volume 1, page 1009, 2012.

[54] L Lepetit, G Cheriaux, and M Joffre. Linear techniques of phase measurement by femtosecond spectral interferometry for applications in spectroscopy. *JOSA B*, 12(12):2467–2474, 1995.

[55] Conor L Evans and X Sunney Xie. Coherent anti-stokes raman scattering microscopy: chemical imaging for biology and medicine. *Annu. Rev. Anal. Chem.*, 1:883–909, 2008.

[56] Hideaki Kano and Hiro-o Hamaguchi. Femtosecond coherent anti-stokes raman scattering spectroscopy using supercontinuum generated from a photonic crystal fiber. *Applied physics letters*, 85(19):4298–4300, 2004.

[57] Hideaki Kano and Hiro-o Hamaguchi. Ultrabroadband (¿ 2500cm- 1) multiplex coherent anti-stokes raman scattering microspectroscopy using a supercontinuum generated from a photonic crystal fiber. *Applied Physics Letters*, 86(12):121113, 2005.

[58] Hideaki Kano. Molecular vibrational imaging of a human cell by multiplex coherent anti-stokes raman scattering microspectroscopy using a supercontinuum light source. *Journal of Raman Spectroscopy*, 39(11):1649–1652, 2008.

[59] Yan-Hua Zhai, Christiane Goulart, Jay E Sharping, Huifeng Wei, Su Chen, Weijun Tong, Mikhail N Slipchenko, Delong Zhang, and Ji-Xin Cheng. Multimodal

coherent anti-stokes raman spectroscopic imaging with a fiber optical parametric oscillator. *Applied physics letters*, 98(19):191106, 2011.

[60] Simon Lefrancois, Dan Fu, Gary R Holtom, Lingjie Kong, William J Wadsworth, Patrick Schneider, Robert Herda, Armin Zach, X Sunney Xie, and Frank W Wise. Fiber four-wave mixing source for coherent anti-stokes raman scattering microscopy. *Optics letters*, 37(10):1652–1654, 2012.

[61] Erin S Lamb, Simon Lefrancois, Minbiao Ji, William J Wadsworth, X Sunney Xie, and Frank W Wise. Fiber optical parametric oscillator for coherent anti-stokes raman scattering microscopy. *Optics letters*, 38(20):4154–4157, 2013.

[62] Andreas Zumbusch, Gary R Holtom, and X Sunney Xie. Three-dimensional vibrational imaging by coherent anti-stokes raman scattering. *Physical Review Letters*, 82(20):4142, 1999.

[63] Winfried Denk, James H Strickler, and Watt W Webb. Two-photon laser scanning fluorescence microscopy. *Science*, 248(4951):73–76, 1990.

[64] YQ Xu, KF Mak, and SG Murdoch. Multiwatt level output powers from a tunable fiber optical parametric oscillator. *Optics letters*, 36(11):1966–1968, 2011.

[65] RT Murray, EJR Kelleher, SV Popov, A Mussot, A Kudlinski, and JR Taylor. Synchronously pumped photonic crystal fiber-based optical parametric oscillator. *Optics letters*, 37(15):3156–3158, 2012.

[66] Lei Jin, Amos Martinez, and Shinji Yamashita. Optimization of output power in a fiber optical parametric oscillator. *Optics express*, 21(19):22617–22627, 2013.

[67] Chenji Gu, Christiane Goulart, and Jay E Sharping. Cross-phase-modulation-induced spectral effects in high-efficiency picosecond fiber optical parametric oscillators. *Optics letters*, 36(8):1488–1490, 2011.

[68] Jay E Sharping, Mark A Foster, Alexander L Gaeta, Jacob Lasri, Ove Lyngnes, and Kurt Vogel. Octave-spanning, high-power microstructure-fiber-based optical parametric oscillators. *Optics express*, 15(4):1474–1479, 2007.

[69] NR Newbury, BR Washburn, KL Corwin, and RS Windeler. Noise amplification during supercontinuum generation in microstructure fiber. *Optics letters*, 28(11):944–946, 2003.

[70] KL Corwin, Nathan R Newbury, JM Dudley, Stéphane Coen, SA Diddams, Karl Weber, and RS Windeler. Fundamental noise limitations to supercontinuum generation in microstructure fiber. *Physical review letters*, 90(11):113904, 2003.

[71] JN Ames, S Ghosh, RS Windeler, AL Gaeta, and ST Cundiff. Excess noise generation during spectral broadening in a microstructured fiber. *Applied Physics B*, 77(2-3):279–284, 2003.

[72] Lin Yi, Xianghui Qi, Wenlan Chen, Jingbiao Chen, Xiaoji Zhou, and Xuzong Chen. Enhancing the signal-to-noise ratio of optical frequency beating using open-loop photonic crystal fiber. *Optics Communications*, 281(15):4081–4087, 2008.

[73] Serguei M Kobtsev and Serguei V Smirnov. Coherent properties of supercontinuum containing clearly defined solitons. *Optics express*, 14(9):3968–3980, 2006.

[74] R Mark Stevenson, Robert J Young, Paola Atkinson, Ken Cooper, David A Ritchie, and Andrew J Shields. A semiconductor source of triggered entangled photon pairs. *Nature*, 439(7073):179–182, 2006.

[75] Markus Müller, Samir Bounouar, Klaus D Jöns, M Glässl, and P Michler. On-demand generation of indistinguishable polarization-entangled photon pairs. *Nature Photonics*, 8(3):224–228, 2014.

[76] RM Stevenson, CL Salter, J Nilsson, AJ Bennett, MB Ward, I Farrer, DA Ritchie, and AJ Shields. Indistinguishable entangled photons generated by a light-emitting diode. *Physical review letters*, 108(4):040503, 2012.

[77] David Fattal. *Single photons for quantum information processing*. PhD thesis, Stanford University, 2005.

[78] CK Hong, ZY Ou, and Leonard Mandel. Measurement of subpicosecond time intervals between two photons by interference. *Physical Review Letters*, 59(18):2044, 1987.

[79] Mark Fox. *Quantum Optics: An Introduction: An Introduction*, volume 6. Oxford university press, 2006.

[80] Magued B Nasr, Bahaa EA Saleh, Alexander V Sergienko, and Malvin C Teich. Demonstration of dispersion-canceled quantum-optical coherence tomography. *Physical review letters*, 91(8):083601, 2003.

[81] AB URen, C Silberhorn, K Banaszek, IA Walmsley, R Erdmann, WP Grice, and MG Raymer. Generation of pure-state single-photon wavepackets by conditional preparation based on spontaneous parametric downconversion. *Laser Physics*, 15(1):146–161, 2005.

[82] WP Grice, AB Uren, and IA Walmsley. Eliminating frequency and space-time correlations in multiphoton states. *Physical Review A*, 64(6):063815, 2001.

[83] K Garay-Palmett, HJ McGuinness, Offir Cohen, JS Lundeen, R Rangel-Rojo, AB U'ren, MG Raymer, CJ McKinstrie, S Radic, and IA Walmsley. Photon pair-state preparation with tailored spectral properties by spontaneous four-wave mixing in photonic-crystal fiber. *Optics express*, 15(22):14870–14886, 2007.

[84] Qiang Zhou, Wei Zhang, Jie-rong Cheng, Yi-dong Huang, Jiang-de Peng, et al. Noise performance comparison of 1.5 μm correlated photon pair generation in different fibers. *Optics express*, 18(16):17114–17123, 2010.

[85] Alex Clark, Bryn Bell, Jérémie Fulconis, Matthäus M Halder, Ben Cemlyn, Olivier Alibart, Chunle Xiong, William J Wadsworth, and John G Rarity. Intrinsically narrowband pair photon generation in microstructured fibres. *New Journal of Physics*, 13(6):065009, 2011.

[86] Karina Garay-Palmett, Alfred B URen, Raúl Rangel-Rojo, Rodger Evans, and Santiago Camacho-López. Ultrabroadband photon pair preparation by spontaneous four-wave mixing in a dispersion-engineered optical fiber. *Physical Review A*, 78(4):043827, 2008.

[87] Krister Shalm, 2015.

[88] Q Lin, F Yaman, and Govind P Agrawal. Photon-pair generation by four-wave mixing in optical fibers. *Optics letters*, 31(9):1286–1288, 2006.

[89] Bin Fang, Offir Cohen, Jamy B Moreno, and Virginia O Lorenz. State engineering of photon pairs produced through dual-pump spontaneous four-wave mixing. *Optics express*, 21(3):2707–2717, 2013.

[90] RH Stolen, MA Bösch, and Chinlon Lin. Phase matching in birefringent fibers. *Optics letters*, 6(5):213–215, 1981.

[91] Brian J Smith, P Mahou, Offir Cohen, JS Lundeen, and IA Walmsley. Photon pair generation in birefringent optical fibers. *Optics express*, 17(26):23589–23602, 2009.

[92] Fabien Boitier, Antoine Godard, E Rosencher, and C Fabre. Measuring photon bunching at ultrashort timescale by two-photon absorption in semiconductors. *Nature Physics*, 5(4):267–270, 2009.

[93] Fabien Boitier, Antoine Godard, Aleksandr Ryasnyanskiy, Nicolas Dubreuil, Philippe Delaye, Claude Fabre, and Emmanuel Rosencher. Second order coherence of broadband down-converted light on ultrashort time scale determined by two photon absorption in semiconductor. *Optics express*, 18(19):20401–20408, 2010.

[94] Barak Dayan, Avi Pe'Er, Asher A Friesem, and Yaron Silberberg. Two photon absorption and coherent control with broadband down-converted light. *Physical review letters*, 93(2):023005, 2004.

[95] Avi Pe'Er, Barak Dayan, Asher A Friesem, and Yaron Silberberg. Temporal shaping of entangled photons. *Physical review letters*, 94(7):073601, 2005.

[96] Chiara Vitelli, Nicolò Spagnolo, Lorenzo Toffoli, Fabio Sciarrino, and Francesco De Martini. Enhanced resolution of lossy interferometry by coherent amplification of single photons. *Physical review letters*, 105(11):113602, 2010.